nature communications

Article

https://doi.org/10.1038/s41467-025-58308-1

Structural insights into the RNA-dependent RNA polymerase complexes from highly pathogenic Marburg and Ebola viruses

Received: 15 August 2024

Accepted: 17 March 2025

Published online: 31 March 2025

Check for updates

Guobao Li[1,4], Tianjiao Du[1,4], Jiening Wang[2,4], Kaiyue Jie[1], Zhuolu Ren[1], Xiaokang Zhang[3], Long Zhang[1], Shan Wu[2,5] ✉ & Heng Ru[1,5] ✉

The Ebola and the Marburg viruses belong to the Filoviridae family, a group of filamentous, single-stranded, negative-sensed RNA viruses. Upon infection, uncontrolled propagation of the Ebola and the Marburg viruses causes severe hemorrhagic fevers with high mortality rates. The replication and transcription of viral genomes are mediated by a polymerase complex consisting of two proteins: L and its cofactor VP35. However, the molecular mechanism of filovirus RNA synthesis remains understudied due to the lack of high-resolution structures of L and VP35 complexes from these viruses. Here, we present the cryo-EM structures of the polymerase complexes for the Marburg virus and the Ebola virus at 2.7 Å and 3.1 Å resolutions respectively. Despite the similar assembly and overall structures between these two viruses, we identify virus-specific L–VP35 interactions. Our data show that intergeneric exchange of VP35 would diminish these interactions and prevent the formation of a functional chimeric polymerase complex between L protein and heterologous VP35. Additionally, we identify a contracted conformation of the Ebola virus polymerase structure, revealing the structural dynamics of the polymerase during RNA synthesis. These insights enhance our understanding of filovirus RNA synthesis mechanisms and may facilitate the development of antiviral drugs targeting filovirus polymerase.

The family *Filoviridae*, which includes Ebola virus (EBOV) and Marburg virus (MARV), is part of the order *Mononegavirales* together with the *Rhabdoviridae*, the *Pneumoviridae*, the *Paramyxoviridae* and the *Bornaviridae* families, etc[1]. EBOV and MARV belong to different filoviral genera, the *Ebolavirus* and *Marburgvirus* respectively, and they are genetically distinct[2]. So far, six species of *Ebolavirus* have been identified, including *Bundibugyo*, *Reston*, *Sudan*, *Taï Forest*, *Bombali*, and *Zaire Ebolavirus*, while *Lake Victoria Marburgvirus* is the only member in *Marburgvirus*[3]. These viruses are enveloped, non-segmented negative-sensed RNA viruses (nsNSVs) capable of causing severe human diseases with potentially fatal outcomes. Among them, MARV and EBOV are notorious for causing filovirus disease (FVD), characterized by severe hemorrhagic fever with up to 90% fatality[4]. Currently, there are no approved drugs or vaccines for these filoviral infections, highlighting the urgent requirements for effective antiviral therapies.

[1]Life Sciences Institute, Second Affiliated Hospital of Zhejiang University School of Medicine, Zhejiang Key Laboratory of Molecular Cancer Biology, Zhejiang University, Hangzhou, China. [2]State Key Laboratory of Biocatalysis and Enzyme Engineering, Hubei Collaborative Innovation Center for Green Transformation of Bio-Resources, Hubei Key Laboratory of Industrial Biotechnology, School of Life Sciences, Hubei University, Wuhan, China. [3]Interdisciplinary Center for Brain Information, The Brain Cognition and Brain Disease Institute, Shenzhen Institute of Advanced Technology, Chinese Academy of Sciences, Shenzhen-Hong Kong Institute of Brain Science-Shenzhen Fundamental Research Institutions, Shenzhen, China. [4]These authors contributed equally: Guobao Li, Tianjiao Du, Jiening Wang. [5]These authors jointly supervised this work: Shan Wu, Heng Ru. ✉e-mail: wushan91@hubu.edu.cn; hengru@zju.edu.cn

The genomes of MARV and EBOV are approximately 19 kb, encoding seven viral proteins in tandem: nucleoprotein (N), viral protein (VP35), VP40, glycoprotein (GP), VP30, VP24, and large protein (L)[2,5,6]. The viral genome is encapsidated by N proteins, forming a helical nucleocapsid that serves as template for replication and transcription[7]. These processes are critical to the viral lifecycle and are facilitated by the RNA-dependent RNA polymerase (RdRp) complex, consisting of the L protein and its essential cofactor VP35, which is analogous to the P protein of other nsNSVs[8,9]. The L protein contains three conserved enzymatic domains essential for the RNA synthesis: the RdRp domain, the polyribonucleotidyl transferase (PRNTase or capping) domain and the methyltransferase (MTase) domain[10,11]. The cofactor VP35 is a multifunctional protein which is not only required for suppression of host innate immune response but also cooperates with the L protein to perform genome replication and mRNA transcription[2,5,12–14]. VP35 has three domains: an N-terminal domain (NTD), a central oligomerization domain (OD) and a C-terminal interferon (IFN)-inhibitory domain (IID)[8,15–17]. The transcription process was assumed to follow a stop–start mechanism, generating each mRNA with a 5′ cap and 3′-polyadenylated tail[2,5,18], while during replication, the polymerase synthesizes a full-length complementary antigenome as an intermediate for genomic RNA production regardless of the transcriptional signal sequences[2,5]. The unique structure, function and catalytic mechanism of the polymerase is highly distinct from host cellular polymerases, making it a promising target for antiviral drug development.

MARV and EBOV share significant similarities in transcription and replication mechanisms[2,5], yet exhibit remarkable differences. Minigenome assays revealed that L, VP35, and NP proteins are essential for replication in both viruses[2,5]. However, EBOV VP30 is required for the transcription initiation at the first gene (N gene)[19] and for GP mRNA co-transcriptional editing[19,20], while MARV VP30 is only needed for transcribing the GP gene (the fourth gene), which does not undergo RNA editing[21]. Another difference lies in the promoter recognition by their respective polymerases, although the 3′-leader or trailer sequences of EBOV are nearly identical to those of MARV. Both MARV and EBOV polymerases could initiate RNA synthesis at +2 position on the EBOV replication promoter[22], while EBOV polymerase cannot initiate RNA synthesis when using the MARV replication promoter[23]. Furthermore, it was shown that exchanging NP, VP35, or L proteins between MARV and EBOV fails to support RNA synthesis[19]. These observations indicate that there may be significant differences in the RNA synthesis machinery between MARV and EBOV genera. In addition, it has been reported that homo-oligomerization via the OD domain is essential for VP35 to perform its cofactor functions[13,16]. Crystallographic studies of VP35 OD have revealed that MARV VP35 (hereafter referred to as mVP35) assembles into a trimer[15], while EBOV VP35 (hereafter referred to as eVP35) assembles into either a trimer or a tetramer[16]. In the reported cryo-EM structures of the EBOV L–VP35 complex, eVP35 forms a tetramer[8,9]. Thus, it is highly interesting to investigate the oligomeric state of mVP35 under the context of the MARV L–VP35 complex as well as to compare the potential similarities and differences in structures and RNA synthesis mechanisms between MARV and EBOV polymerases. In addition, the reason why heterologous VP35 cannot function as the cofactor of L to exert its polymerase activity remains unknown.

In this study, we resolved the cryo-EM structures of the MARV and EBOV polymerases at resolutions of 2.7 Å and 3.1 Å, respectively, and both structures adopt as an elongation state. Although EBOV and MARV polymerases share a similar binding pocket for the anti-EBOV compound suramin, its affinity for MARV polymerase is significantly lower, suggesting potential structural differences between the two. In addition, our study reveals both conserved and virus-specific L–VP35 interactions between MARV and EBOV. Exchanging VP35 would impairs these specific interactions and prevents the formation of a functional chimeric polymerase complex between L protein and heterologous VP35. Furthermore, we also identified a distinct contracted conformation of the EBOV polymerase, implying the structural dynamics of the polymerase during RNA synthesis. These insights not only enhance the comprehensive understanding of the replication and transcription mechanisms of filovirus polymerases but also pave the way for the development of antiviral drugs targeting these RdRp complexes.

Results

Cryo-electron microscopy structure determination

In order to obtain a soluble and well-behaved MARV and EBOV L–VP35 complex samples suitable for structure determination, we chose the following constructs: C-terminally maltose binding protein (MBP) and Flag-tagged MARV L (hereafter referred to as MARL), and N-terminally His_6-MBP-tagged mVP35 for MARV L–VP35 complex; N-terminally Strep-MBP-tagged and C-terminally FLAG-tagged EBOV L (hereafter referred to as EBOL), and N-terminally His_6-MBP-tagged eVP35 for EBOV L–VP35 complex (Supplementary Fig. 1a, b). In addition, we also constructed the core regions comprising only the RdRp and PRNTase domains of MARL and EBOL to co-express with their cognate N-terminally truncated VP35 (Supplementary Fig. 1c, d). These combinations of constructs were co-expressed individually in Sf9 insect cells and the L–VP35 complexes purified through FLAG- or Strep-affinity columns were finally homogenized by size exclusion chromatography and analyzed by SDS-PAGE prior to subsequent structural studies (Supplementary Fig. 1a–d). Additives including CHAPS or trehalose were applied during the vitrification process to partially alleviate the denaturing of the complex adsorbed at the air–water interface when necessary[24,25].

We collected a large number of cryo-EM images for the L–VP35 complexes of MARV and EBOV, and two-dimensional (2D) averages displayed a distribution of the molecules with different projection angles. 2D-cleaned particles were then subjected to ab-initio reconstruction and multiple rounds of heterogeneous refinement in cryoSPARC (Supplementary Fig. 2–4). For the full-length MARV L–VP35 construct (hereafter referred to as $(L–VP35)_M^{FL}$), only one map produced by the heterogeneous 3D classification could be further refined to 2.7-Å resolution (Fig. 1a, Supplementary Fig. 2a–e). For the full-length EBOV L–VP35 construct, we were unable to obtain an unambiguous cryo-EM map due to the aggregation of the particles during the vitrification process. In addition, we also obtained the cryo-EM maps for the L–VP35 complexes of MARV and EBOV core regions by using C-terminally truncated L and N-terminally truncated VP35 (hereafter referred to as $(L–VP35)_M^{Core}$ and $(L–VP35)_E^{Core}$, respectively) at 2.8- and 3.1-Å resolution, respectively, following similar data processing procedures (Supplementary Fig. 3a, 4a). Atomic models were built into these high-resolution maps and were further refined iteratively in the real and reciprocal spaces (Fig. 1b, Supplementary Fig. 5–9 and Supplementary Table 1).

Overview of MARV and EBOV L–VP35 maps and models

The final map/model of $(L–VP35)_M^{FL}$ is nearly identical to that of the $(L–VP35)_M^{Core}$ with a root mean square deviation (R.M.S.D.) less than 0.3 Å (Fig. 1a and Supplementary Fig. 8). Since the cryo-EM map of $(L–VP35)_M^{FL}$ is of better resolution, we employ this map/model for subsequent dissection. The final model of $(L–VP35)_M^{FL}$ consists of one MARL protein and four mVP35 molecules. The MARL protein includes only the RdRp and PRNTase domains (encompassing conserved regions I to V), while residues from position 1416 to the C-terminus—comprising the connection, methyltransferase (including conserved region VI), and C-terminal domains—lack density in the cryo-EM map. (Fig. 1b, c). In addition, four mVP35 molecules with different lengths form a tetramer through its OD, which tightly grips the funnel-like core region of the MARL protein (Fig. 1b, d). The missing parts in the MARL

https://doi.org/10.1038/s41467-025-58308-1

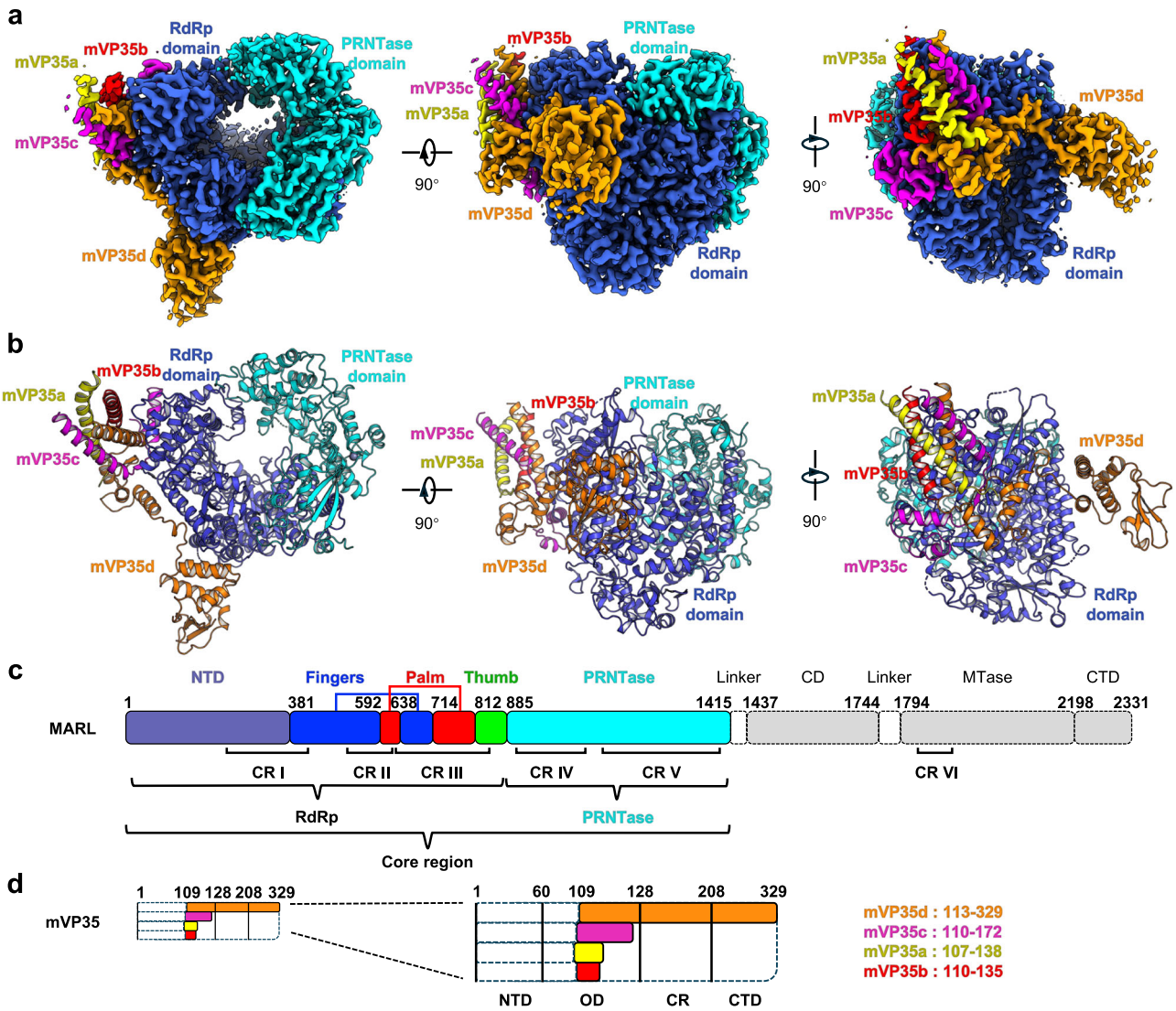

Fig. 1 | Overview of the map and model of MARV L–VP35 complex. a Orthogonal view of the cryo-EM map of MARV L–VP35 complex. Visible domains in the map of MARL including the RNA-dependent RNA polymerase (RdRp) domain and the polyribonucleotidyl transferase (PRNTase or capping) domain as well as four mVP35 protomers have been labeled on the map. The resolved RdRp and PRNTase domains are depicted in slate and cyan, respectively. The four mVP35 protomers with different lengths are shown in different colors: mVP35a is shown in yellow, mVP35b in red, mVP35c in magenta, and mVP35d in orange. **b** Cartoon representation of MARV L–VP35 complex. MARL and mVP35 are colored as in **a**. **c, d** Domain organization of MARL and mVP35. The RdRp domain consists of four subdomains, and they are colored as follows: the N-terminal domain (NTD) is shown in slate, fingers in blue, palm in red, and thumb in green. The densities for the connection domain (CD), methyltransferase (MTase) domain, and C-terminal domain (CTD) are missing in the cryo-EM map and thus are shown in gray. Six conserved regions (CR I–VI) of MARL are labeled based on the sequence alignment of the representative nsNSVs. mVP35 consists of four domains: N-terminal domain (NTD), oligomerization domain (OD), connection region (CR), and C-terminal domain (CTD). mVP35 protomers are colored as in **a**.

and mVP35 molecules are not due to degradation of these regions in the protein sample (Supplementary Fig. 1a) but rather may be attributed to their intrinsic flexibility relative to the core of the complex. The cryo-EM map/model of our $(L–VP35)_E^{Core}$ at 3.1 Å resolution resembles the previously published EBOV polymerase complexes (Supplementary Fig. 9), in which the full-length EBOL protein was utilized but the accessory domains were also missing in the cryo-EM maps[8,9].

The similarity among the structures of $(L–VP35)_M^{FL}$, $(L–VP35)_M^{Core}$ and the previously published EBOV L–VP35 complexes[8,9] (Fig. 1a, b and Supplementary Fig. 8, 9) suggests that the assembly of the polymerase complexes is highly conserved among the filovirus family. In fact, the overall architectures of the MARV and EBOV L–VP35 complexes are analogous to that of other polymerase complexes determined in nsNSVs. Comparison of the L–VP35 core structure of MARV and EBOV with that of vesicular stomatitis virus (VSV)[26,27], rabies virus (RABV)[28], parainfluenza virus type 5 (PIV5)[29], Newcastle disease virus (NDV)[3], human parainfluenza virus type 3 (hPIV3)[30], mumps virus (MuV)[31], human metapneumovirus (HMPV)[32], respiratory syncytial virus (RSV)[33–35] and EBOV[8,9] results in an R.M.S.D. ranging from 1.6–3.0 Å (Supplementary Fig. 10), indicating that the core structures of the polymerase complexes are highly conserved during the evolution of nsNSVs.

However, the ODs of mVP35 and eVP35 observed in our maps are much shorter than those in the published EBOV polymerase structures (Fig. 1a, b and Supplementary Fig. 8–10). Accordingly, a turn could be observed in the OD region of mVP35 in some representative 2D projections of the MARV polymerases (Supplementary Fig. 2b, 3b), reflecting the intrinsic flexibility of this region, which may account for the difficulty in the reconstruction of the complete mVP35 OD within the MARV polymerase structures. Although the OD of eVP35 appears relatively straight in some 2D class averages of $(L–VP35)_E^{Core}$ (Supplementary Fig. 4b), the oscillation of eVP35 OD

region was observed in the L–VP35 structures of EBOV in both the RNA-free and -bound forms[8,9]. Consistent with this, the missing part in the eVP35 OD in our $(L–VP35)_E^{Core}$ structure may be attributable to structural vibrations. Collectively, these results indicate that the filoviral VP35 ODs are highly dynamic and may play particular roles in the processes of RNA synthesis and pathogenesis during viral propagation.

Structural features of the RdRp domain of MARV L protein

The RdRp domain of nsNSVs is responsible for viral RNA synthesis[11,36]. The RdRp domain of MARL protein exhibits a classical right-handed finger–palm–thumb architecture, similar to many RNA polymerase structures[11,36] (Fig. 2a and Supplementary Fig. 11a–g). The RdRp domain comprises six conserved motifs (A–F), with motifs A–E positioned in the palm subdomain and motif F protruding from the fingers subdomain (Fig. 2b and Supplementary Fig. 12a). These motifs contain conserved amino acid residues that are critical for catalyzing RNA synthesis. The GGxxG sequence in motif B and the conserved glycine residue (G812) in motif E flank the palm subdomain (Fig. 2b), implying their potential role in supporting the flexibility of the palm subdomain during RNA synthesis. Motif C carries the highly conserved ^{744}GDN^{746} motif within the β-turn connecting β10 and β11 of MARL (Fig. 2b, Supplementary Fig. 13). Structural superposition of the palm subdomain of hepatitis C virus (HCV) RNA polymerase (PDB: 1NB6) to that of MARL suggests that the ^{744}GDN^{746} motif together with the residue D635 from motif A may play a role in coordinating two magnesium ions, which are required for catalyzing the formation of phosphodiester bonds through a potential "two-metal-catalysis" mechanism (Fig. 2b, c). Although magnesium ions were included during the purification process, the densities for the ions couldn't be observed in the active site of the RdRp domain, possibly due to lack of the other binding ligands, i.e. RNA or NTP substrates.

Comparison the RdRp domain of MARV with those of VSV, RABV and EBOV uncovers an insertion element around 37 amino acid residues between β3 and β4 in the NTD subdomain of MARL, which is similar to that of EBOV, except that the insertion element consists of four α-helices in MARL while three helices in EBOL (Fig. 2d and Supplementary Fig. 14a, b). Despite sharing some sequence similarity in the insertion element (Supplementary Fig. 11j), the R.M.S.D. of the insertion between MARV and EBOV is about 4.4 Å based on the superposition of Cα residues (Supplementary Fig. 11h). Structural-based sequence alignment revealed that the insertion element is filovirus-specific among nsNSVs (Supplementary Fig. 11j). In addition, filoviruses and other nsNSVs lack an α-helix and β-strand structure prior to the β-sheet in the NTD, which is rhabdovirus-specific (Fig. 2d and Supplementary Fig. 14c, d). In EBOV, removal of the insertion element from the L protein abolishes its transcription activity[8]. The insertion element in EBOL and MARL seems to play a role in stabilizing the surrounding residues mainly through hydrophobic interactions and is important for structural integrity of the L protein (Supplementary Fig. 11i).

Suramin has been reported to be a potent non-nucleoside inhibitor for several viruses, including norovirus[37], SARS-CoV-2[38] and EBOV[8], by occluding the NTP entry channel of the viral polymerase. Superposition of the RdRp structures of MARL and suramin-bound EBOL (PDB: 7YET) revealed that residues involving in the polar and hydrophobic interactions with the inhibitor in EBOL are almost conserved in MARL (Fig. 2e). Of note, F793 in EBOL experiences conformational change upon suramin binding, whereas the corresponding residue F796 in MARL already adopts the bound conformation (Fig. 2e). In order to evaluate whether suramin has potential inhibitory effect on the activity of MARV polymerase, we first measured the binding affinity of both EBOV and MARV polymerases to suramin by microscale thermophoresis (MST) binding assay. Unexpectedly, the binding affinity of suramin to MARV polymerase was much lower than that to EBOV polymerase no matter under near-physiological (11.1 ± 3.8 μM) or high-salt conditions (17.3 ± 3.1 μM) (Fig. 2f). This reduced binding affinity may be attributed to a subtle mismatch between part of the suramin molecule and the MARV polymerase binding pocket, or to the absence of the other half of the suramin molecule in the EBOV polymerase structure (PDB: 7YET), which might hinder effective binding to the MARV polymerase. Considering that inhibition relies on initial binding to the target, we speculate that the ability of suramin to suppress MARV polymerase activity is likely to be significantly compromised.

Both MARV and EBOV L proteins adopt an elongation conformation

The PRNTase domain is responsible for the addition of a 5′ cap structure to the nascent viral mRNAs during transcription[39]. Like other nsNSVs, the PRNTase domain of MARV and EBOV contains five highly conserved motifs (motif A′–E′) (Fig. 2g and Supplementary Fig. 12b). The motif B′, also known as the priming loop (encompassing residues 1211–1238 in MARL) and thought to facilitate de novo initiation[11,36], is partially missing in our structure (Fig. 2g, h). The priming loop is completely missing in EBOL at state 1, while it is visible at state 2 and also partially observed in the EBOV L–VP35 structure in complex with a 3′-leader RNA (Fig. 2h), which correspond to the elongation and initiation conformation, respectively[8]. The trajectories of the priming loops in both MARL and EBOL, as determined here, resemble those of the previously published EBOL structure at state 2 and in its RNA-bound form (Fig. 2h and Supplementary Fig. 15a, b).

The RdRp and PRNTase domains tightly associate with each other to constitute the core of L proteins. Two loops in the PRNTase domain, the priming loop and the intrusion loop, perform different functions during the RNA synthesis process. The priming loop (motif B′) has been reported to play an important role in stabilizing the initiation NTP through a ring-based priming residue during de novo initiation at the 3′ terminus of the template in a number of nsNSVs[11,36,39], while the intrusion loop plays a distinct role. Both loops can occupy or move away from the central cavity according to the different stages of RNA synthesis[10,11,36]. In the polymerase structures of rhabdoviruses, the priming loops are deeply inserted into the central cavity and close to the active sites of RdRp domains while the intrusion loops are retained in the PRNTase domains, which is considered to be an initiation conformation[26,28] (Fig. 3a). In addition, in the polymerase structures of PIV5, NDV, hPIV3 and MuV, the priming loops are retracted whereas the intrusion loops are positioned in the central cavity, which is assumed to be a post-initiation conformation[3,29–31] (Fig. 3b and Supplementary Fig. 15c). Furthermore, in the RSV, HMPV, and EBOV polymerase structures, both loops either withdraw from the central cavity or are missing, indicating an elongation conformation[8,32–34] (Fig. 3c and Supplementary Fig. 15d). What's more, conformational changes are also observed in the supporting helix of the palm subdomain. In L proteins observed in the initiation (VSV and RABV)[26,28] or in the post-initiation states (PIV5, NDV, hPIV3, and MuV)[3,29–31], the supporting helices obstruct the RNA product exit channels, thereby blocking the RNA elongation (Fig. 3a, b and Supplementary Fig. 15c). In contrast, the supporting helices in L proteins in the non-initiation/elongation state (such as HMPV and EBOV) are shifted away or even absent (as observed in RSV), allowing the growing RNA to pass through the exit channel (Fig. 3c and Supplementary Fig. 15d). Recently, the cryo-EM structures of EBOV and RSV polymerase in complex with RNA promoters in the pre-initiation state have been reported[9,35]. However, the positions of the priming and intrusion loops are nearly identical to those in the previously published elongation state (Fig. 3d and Supplementary Fig. 15e). The MARV and EBOV polymerase structures solved here exhibit retracted intrusion loops and partially visible

https://doi.org/10.1038/s41467-025-58308-1

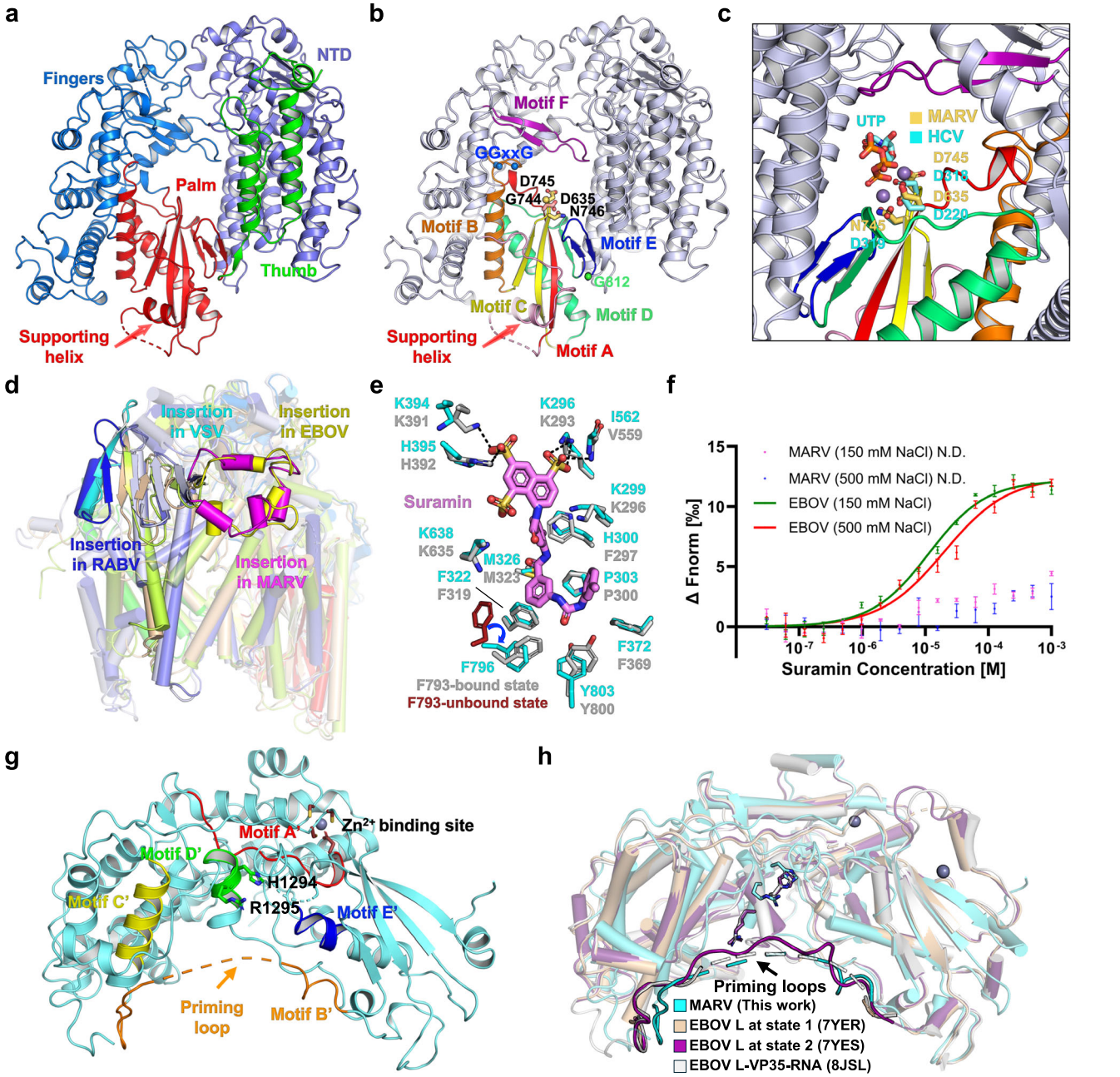

Fig. 2 | Structural features of the RdRp and PRNTase domains of MARV L. **a** Structure of the RdRp domain of MARL. The RdRp domain is depicted in ribbon and colored by subdomains as in Fig. 1c. **b** Six catalytic motifs (A–F) in the RdRp domain are highlighted: motif A (red), B (orange), C (yellow), D (green), E (blue), and F (purple). Catalytic residues, Asp635 from motif A and the ^{744}GDN^{746} cluster from motif C, are displayed as sticks (Asp635, Asp745 and Asn746) or sphere (Gly744 Cα). The conserved GGxxG motif and residue G812 flanking the palm subdomain are shown as blue and green spheres, respectively. **c** Close-up of the catalytic center alignment of palm subdomains from MARV and HCV (PDB: 1NB6). Docked UTP and two Mn^{2+} are based on the superposition of catalytic residues shown in yellow and cyan sticks, respectively. **d** Comparison of insertion elements in L proteins from VSV (PDB: 5A22), RABV (PDB: 6UEB), EBOV (PDB: 7YER) and MARV. The insertion elements in VSV and RABV are colored in cyan and blue, while those of MARV and EBOV are colored in magenta and yellow. **e** Suramin docking into MARL using EBOV L–VP35 (PDB: 7YET) as a model. Binding pockets are shown with MARL and EBOL residues as cyan and gray sticks. Polar interactions in EBOL are in black dashed lines, and Phe793 in apo-form EBOL (PDB: 7YER) is in dark red. **f** MST analysis of the suramin binding to MARV and EBOV polymerases. Binding curves and the K_d values are shown under 150 mM and 500 mM NaCl. N.D. indicates no binding within the experimental concentration range. Data are presented as ± S.D. of the mean, $n = 3$ biologically independent measurements. Raw data are provided as a Source Data file. **g** Five conserved PRNTase motifs (A′–E′) in MARL are colored: A′ (red), B′ (orange), C′ (yellow), D′ (green), and E′ (blue). Part of motif B′ (the priming loop) is missing. Conserved catalytic residues, ^{1294}HR^{1295} in the motif D′ are shown as green sticks and the Zn^{2+} binding site is highlighted. **h** Comparison of the priming loops from MARV and EBOV at different states. The PRNTase domains are colored with priming loops indicated by a black arrow.

priming loops, positioned in a way that is unlikely to extend into the central cavity (Figs. 2g, 3c and Supplementary Fig. 15a). Additionally, the supporting helix is displaced from the RNA exit channel (Fig. 3c). These features, similar to those observed in the published RSV, HMPV, and EBOV structures[8,9,33,34], along with the absence of the RNA promoter for structural determination, suggest that the MARV and EBOV polymerase structures presented herein are in an elongation state.

https://doi.org/10.1038/s41467-025-58308-1

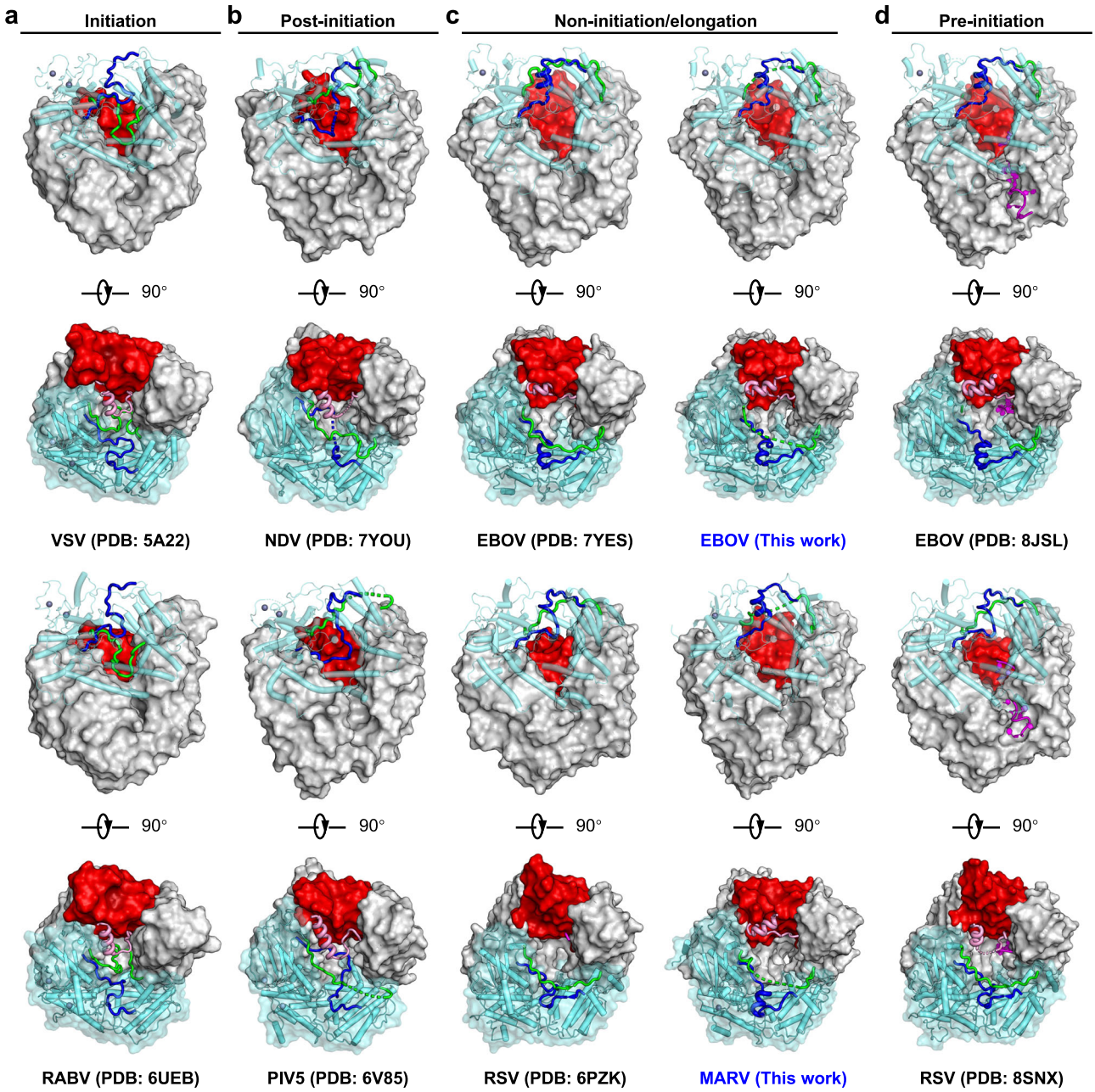

Fig. 3 | Comparison of the positions of the priming loops, intrusion loops and supporting helices among different nsNSV polymerases at different states. Different positions of priming loops, intrusion loops, and supporting helices in the polymerase structures at various states are shown from side and top views, including the initiation (**a**), post-initiation (**b**), non-initiation/elongation (**c**), and pre-initiation (**d**) states. The CD, MTase and CTD of VSV (PDB: 5A22), RABV (PDB: 6UEB), NDV (PDB: 7YOU) and PIV5 (PDB: 6V85) are hidden for clarity. The RdRp domains are shown as surfaces in light gray, with the palm subdomains highlighted in red. The PRNTase domains are shown as transparent surfaces with the cartoons colored in cyan (top view). The supporting helices from palm subdomains and the priming and intrusion loops from PRNTase domains are highlighted in pink, green and blue, respectively. The RNA promoters bound to EBOV (PDB: 8JSL) and RSV (PDB: 8SNX) are colored in magenta.

Superposition of our $(L–VP35)_M^{FL}$ structure with the EBOV L–VP35 structure in complex with a 3′-leader RNA (PDB: 8JSL) revealed that the leader RNA could be appropriately accommodated into the template entry channel of the MARV polymerase (Supplementary Fig. 16a). The corresponding RNA-binding residues are highly conserved and located in the similar positions in MARV polymerase (Supplementary Fig. 16b–d). Furthermore, these residues are highly conserved across different genera of the filovirus family (Supplementary Fig. 16e). These findings, along with the conservation of leader and trailer sequences in their RNA genomes (Supplementary Fig. 16f), suggest a common mechanism by which filoviral polymerases capture the ends of template RNAs.

Structure of EBOV polymerase in a distinct conformation

As mentioned above, the overall architecture of the $(L–VP35)_E^{Core}$ comprising only the core region of EBOL within the construct is similar to the published EBOV L–VP35 structures in the apo state (PDB: 7YER and 7YES) or in complex with a 10 nt 3′-leader RNA (PDB: 8JSL), in which full-length EBOL proteins were included for structural determination[8,9]. However, the overall R.M.S.D.s between our

https://doi.org/10.1038/s41467-025-58308-1

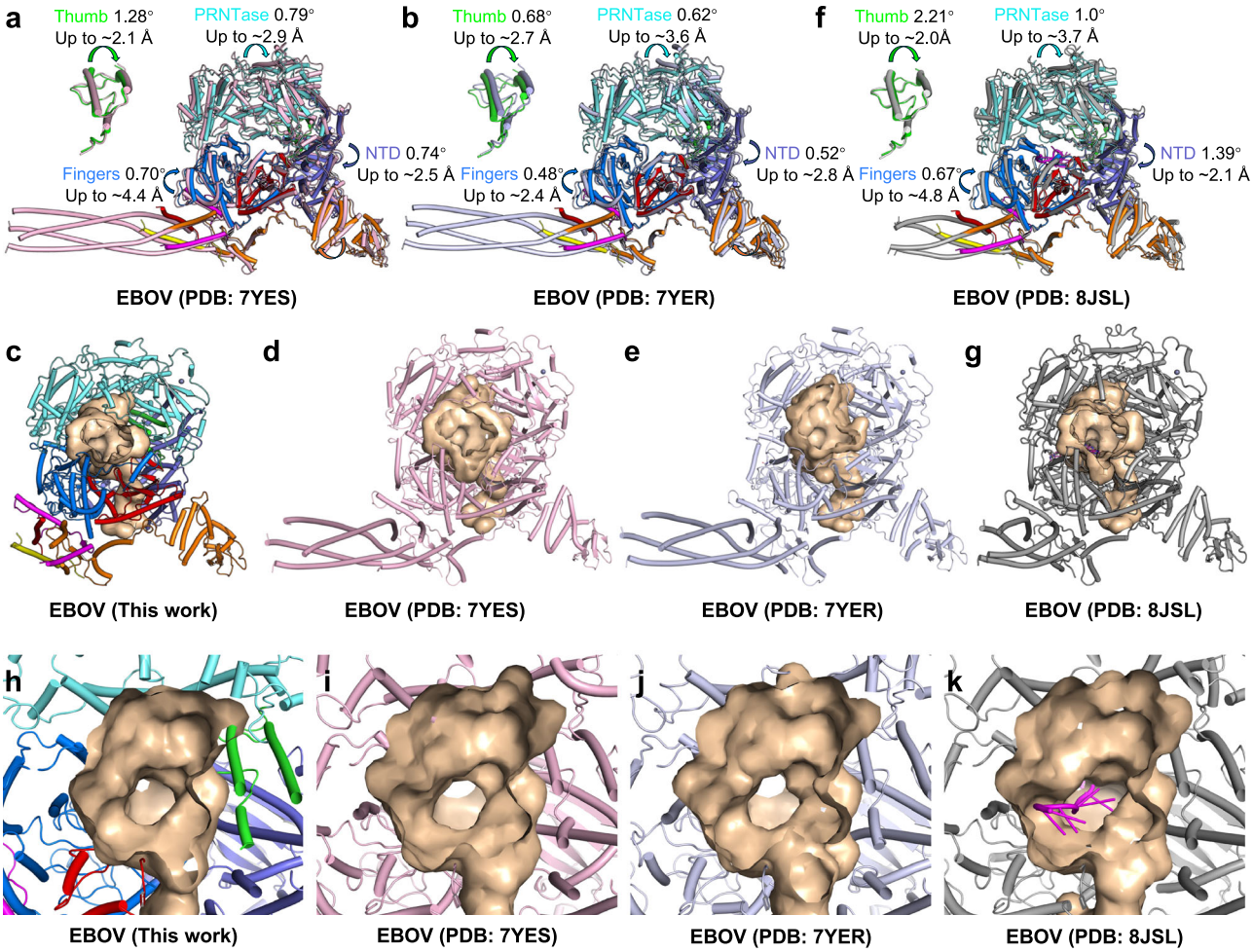

Fig. 4 | Different conformations of EBOV polymerase complexes. a, b, f Structural comparisons of the EBOV polymerase from this study with previously published structures (PDB: 7YES, 7YER and 8JSL) based on the alignment of the palm subdomains. The EBOL model from this study is color-coded by (sub)domains: NTD (slate), fingers (blue), palm (red), thumb (green), and PRNTase (cyan). The previously published EBOV polymerase structures (PDB: 7YES, 7YER and 8JSL) are colored in pink, light blue and gray, respectively. Relative rotation angles and translation distances of each (sub)domain are indicated. **c–e, g** Central cavity spaces of EBOV polymerases are visualized as wheat-colored volumes. **h–k** Close-up views of the promoter RNA entry channels in the EBOV polymerase structures are visualized as wheat-colored volumes.

$(L\text{–}VP35)_E^{Core}$ structure and these solved structures are greater than 1.5 Å (Supplementary Fig. 17a–c), despite nearly identical sequences in these models. In contrast, the R.M.S.D. between $(L\text{–}VP35)_M^{FL}$ and the published EBOV polymerase structures in the elongation state is below 1.4 Å despite lower sequence identity (Supplementary Fig. 13 and Supplementary Fig. 17d–e), indicating that the conformation of $(L\text{–}VP35)_E^{Core}$ we have obtained here is different from that of MARV or the previously published EBOV polymerase structures.

Comparison of our $(L\text{–}VP35)_E^{Core}$ structure with the EBOV L–VP35 structure in the elongation state (PDB: 7YES and 7YER) revealed noticeable positional shifts across the domains. By aligning their catalytic palm subdomains, we observed that the rest of the subdomains from the RdRp domain (NTD, fingers and thumb), along with the PRNTase domain and the attached VP35 tetramer, exhibited very slight rotations relative to those in the published EBOV L–VP35 structures, which results in the inward movement of each (sub) domains by approximately 2.0 to 4.8 Å (Fig. 4a, b and Supplementary Fig. 18a–e). This movement resulted in the contraction of the central cavity with a reduced space (Fig. 4c–e). However, each (sub)domains could be well-aligned individually (Supplementary Fig. 18f–j), illustrating that the structural changes of each (sub)domain are primarily due to rigid-body movement among the domains rather than internal rearrangements. Similar conformational changes were observed between our $(L\text{–}VP35)_E^{Core}$ and the EBOV L–VP35–RNA structure (PDB: 8JSL) (Fig. 4f, g and Supplementary Fig. 18a–e). Additionally, the inward movement of the NTD, fingers and PRNTase domains leads to a narrowing of the template RNA entry channel compared with the previously published EBOV L–VP35 structures (Fig. 4h–k), and creates steric hindrance between the bound RNA and residues in the template entry channel of our $(L\text{–}VP35)_E^{Core}$ structure (Supplementary Fig. 19a), implying that conformational changes are necessary to accommodate the engagement of template RNA during catalysis. In addition, an RNA duplex can be well positioned within the central cavity of the MARV and EBOV L proteins (Supplementary Fig. 19b, c). Therefore, our $(L\text{–}VP35)_E^{Core}$ structure unveils a distinct conformation of the polymerase in the elongation state, although its biological significance during catalysis remains elusive.

Interactions between MARV L and VP35

The association of the cofactor VP35 is critical for the filovirus L protein to fulfil its RNA synthesis activities[2,5,8,9]. The mVP35 tetramer grips on MARL in a tentacular manner, with each protomer adopting a unique conformation (Fig. 5a, b). The interaction between mVP35 and MARL involves both polar and hydrophobic contacts, encompassing a totally buried surface area of approximately 3645 $Å^2$ (Fig. 5c). Within the mVP35 tetramer, the two shorter molecules, mVP35a (residues

https://doi.org/10.1038/s41467-025-58308-1

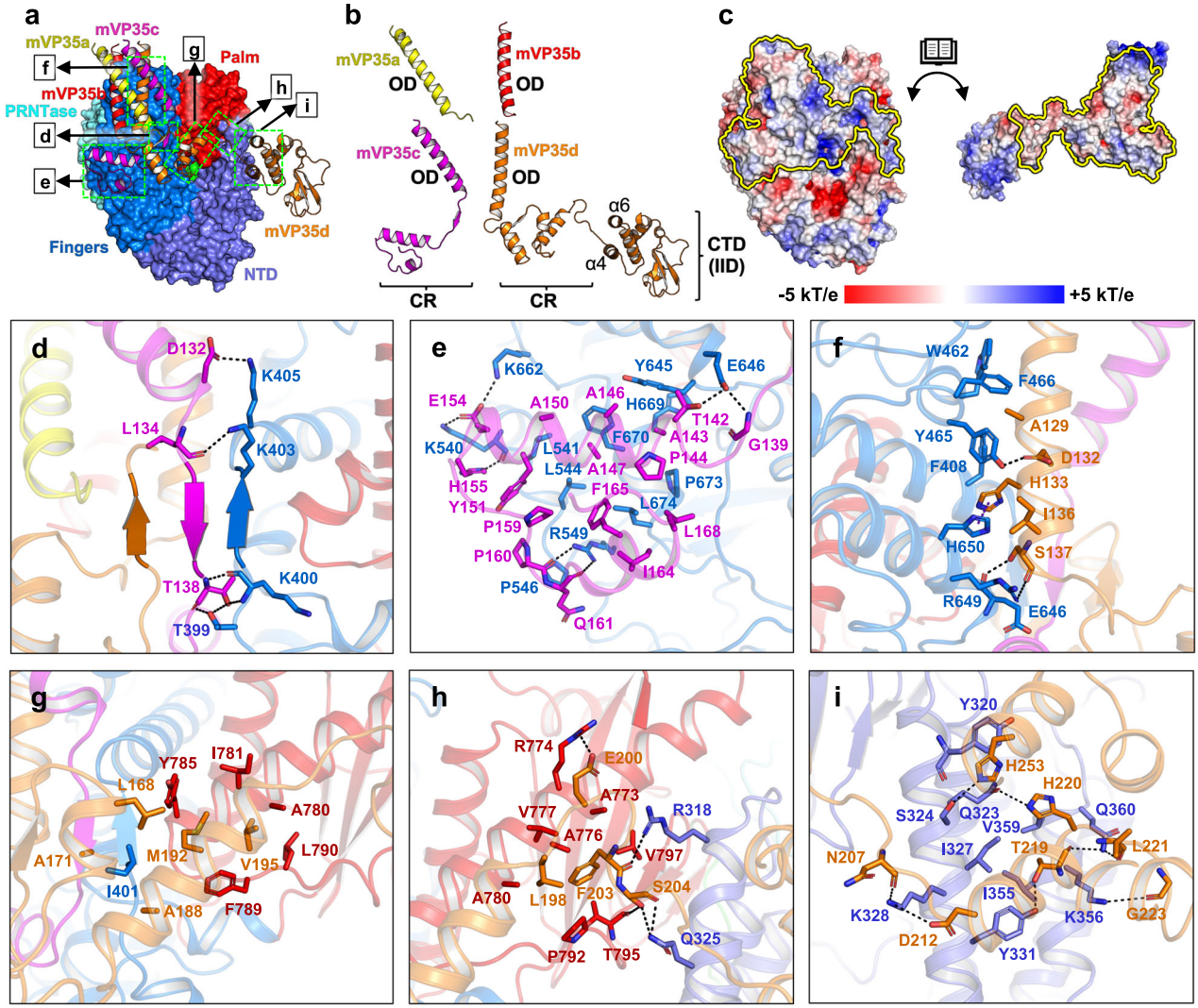

Fig. 5 | Interaction between MARV L and VP35 tetramer. a Surface representation of interaction between MARL and mVP35 tetramer. MARL is shown as molecular surfaces and colored by domains. mVP35 tetramer is shown by ribbons and colored by protomers. The interaction interfaces from **d**–**i** are indicated. **b** Different conformations of mVP35 protomers in the tetramer. The domains of mVP35 are indicated in the structures, including the oligomerization domain (OD), connection region (CR) and C-terminal domain (CTD) or interferon inhibitory domain (IID). **c** The interaction interface of MARL and VP35 tetramer are shown by surface electrostatic potentials, which were calculated by the APBS Electrostatics Plugin of PyMOL. The interaction interface is displayed in an open-book view. The approximate binding surface is outlined in yellow. **d**–**i** Detailed interactions between MARL and mVP35 from different regions as labeled in **a**. The main chains or side chains involved in hydrogen bonding, salt bridge, π–π stacking interactions and hydrophobic interactions are shown as sticks. Hydrogen bonds and salt bridges are shown by black dashed lines and the π–π stacking interactions is indicated by purple dashed lines.

107–138) does not contact with L, while mVP35b (residues 110–135) forms a hydrogen bond with MARL through T116 of mVP35b and H437 from MARL (Supplementary Data 1). The other two protomers, mVP35c (residues 110–172) and mVP35 d (residues 113–329), contribute to the majority of the interactions with MARL (Supplementary Data 1). mVP35c only contacts with the fingers subdomain through the connection region (CR), whereas the longest molecule, mVP35d, forms tripartite interactions with the NTD, fingers, and palm subdomain of MARL (Fig. 5a).

Additionally, the regions immediately following the ODs of mVP35c (residues 135–137) and the CR of mVP35d (residues 163–165) form a three-stranded β-sheet together with the region from the fingers subdomain (residues 400–402). Residues flanking both β-strands of mVP35c and MARL that generate extensive polar interactions, reinforcing the ODs of mVP35 tetramer to firmly grasp the fingers of MARL (Fig. 5d). Subsequent to the β-strand of mVP35c, the remaining CR of mVP35c is composed of two α-helices (α1, residues 141–155 and α2, residues 163–168) (Fig. 5a, b), with numerous hydrophobic interactions and a few polar contacts observed between these two helices and the fingers subdomain of MARL (Fig. 5e).

Intriguingly, the OD helix of mVP35d (residues 113–138) extends slightly longer than those of the other three mVP35 protomers (Fig. 5b), and it is situated closest to the fingers of MARL, facilitating more interactions between them (Fig. 5f). Specifically, residue A129 from mVP35d inserts into a hydrophobic pocket formed by residues F408, W462, F466, and Y465 of MARL. In addition, the side chain of residue D132 forms a hydrogen bond with that of Y465 from MARL (Fig. 5f), and the residue H133 engages in π–π stacking with residue H650 of MARL (Fig. 5f). The main chain of I136 and the side chain of S137 establish hydrogen bonds with the side chain of R649 and main chain of E646 from MARL, respectively (Fig. 5f), which stabilize the helical extension of mVP35d up to T138 and further strengthen the interactions between mVP35d and MARL.

In contrast to mVP35c, the corresponding residues in the CR of mVP35d adopt a distinct arrangement, sequentially forming an α-helix (residues 145–155), a β-strand (residues 163–165), and another short α-

helix (residues 168–172) (Fig. 5b). These conformational differences demonstrate the intrinsic structural flexibility and plasticity of mVP35. The entire mVP35d CR and the C-terminal IID are successfully constructed in our structure (Fig. 5a, b). In mVP35d CR, two α-helices (α1, residues 168–172, and α2, residues 184–196) interact with MARL primarily through hydrophobic interactions (Fig. 5g). The subsequent loop (residues 197–209) wraps around the NTP entry channel (Fig. 5a, h). Notably, F203 inserts into a hydrophobic pocket formed by residue L198 of mVP35d and residues A776, V777, I778, L790, P792 and V797 from MARL (Fig. 5h). Furthermore, polar interactions among residues E200, S204, and N207 of mVP35d, and residues R774, Q325, T795, and K328 of MARL further enhance the structural stability of the NTP entry channel (Fig. 5h).

mVP35d IID domain binds to MARL NTD through two α-helices (α4, residues 210–220, and α6, residues 245–258) with a relatively smaller interface around 720 Å^2 (Fig. 5a, b). The side and main chains of residue T219 from mVP35d establish hydrogen bond interactions with the side chains of Y331 and Q360 of MARL, respectively (Fig. 5i). In addition, the hydrophobic methyl group of mVP35d T219 inserts into the hydrophobic pocket formed by residues I327, I355 and V359 of MARL. Furthermore, hydrogen bonds are observed among residues D212, L221, and H253 of mVP35d and residues K328, Q360, and S324 of MARL, respectively, further facilitating the attachment of mVP35d IID to MARL (Fig. 5i). Removing IID from mVP35 couldn't abolish its interaction with MARL (Supplementary Fig. 20a, b). However, the supplying of IID through co-expression fails to rescue the formation of an intact polymerase complex due to its relatively low binding affinity for MARL (Supplementary Fig. 20c), and complexes lacking the mVP35 IID are eluted in the void volume of gel filtration column, indicative of a high degree of aggregation of the incomplete complex (Supplementary Fig. 20d). These findings underscore the critical role of the IID of VP35 in maintaining the stability and integrity of the L–VP35 complex. Moreover, this assay also mimics scenarios where mutations impairing the interaction between VP35–OD or VP35–IID and L could severely compromise the functionality of the polymerase.

Structural basis of functional incompatibility of intergeneric L–VP35 interaction

The MARV and EBOV polymerase complexes exhibit a high degree of sequence identity (47% for L protein and 36% for VP35) (Supplementary Fig. 13, 21) and overall structural similarity (Supplementary Fig. 17), however, it has been reported that interchanging VP35 between MARV and EBOV fails to support the viral RNA synthesis function of L proteins[19]. In order to investigate whether it is attributed to the inability of VP35 to bind to heterologous L protein or the chimeric complex is inactive, we conducted co-expression and pull-down experiments using different combinations of L–VP35 pairs. As is shown in Supplementary Fig. 22, the yields of the polymerase complexes were significantly reduced in the groups expressing L and heterologous VP35 compared to those expressing homologous protein pairs, although the expression levels of L and VP35 were comparable in each group. This indicates that L protein has decreased affinity for heterologous VP35 and the binding of VP35 to its cognate L protein is required for the assembly of a stable and intact polymerase complex, which could be crucial to the enzymatic activity of the L protein.

To understand why heterologous polymerase complexes are disfavored, we compared the L–VP35 interaction interfaces of MARV and EBOV. Despite the overall L–VP35 R.M.S.D. being ~1.4 Å, structural alignment of the eVP35 OD and CR with mVP35 (R.M.S.D. ~0.8 Å) revealed an outward shift in eVP35 IID, with α4 and α6 moving outward by 1–2 Å and 2–3 Å, respectively (Fig. 6a). This shift requires the IID of eVP35 to rotate ~6.5° to align with mVP35 IID (Fig. 6a). Since VP35 IID contacts L NTD via α4 and α6 (Fig. 5a, i), this outward movement weakens their interaction when eVP35 OD and CR are attached (Fig. 6a). Similarly, alignment of eVP35 IID with mVP35 IID (R.M.S.D. ~0.7 Å) revealed an inward shift of eVP35 OD and CR by ~7–8 Å, necessitating a ~4.5° rotation for alignment (Fig. 6b). This inward movement creates severely steric hindrance with MARV L, hindering the association of eVP35 OD and CR with MARV L (Fig. 6b).

Detailed comparison of the L–VP35 interaction interfaces in MARV and EBOV revealed high conservation in most regions, including the VP35c CR–L fingers subdomain and VP35d OD–L fingers subdomain interfaces (Fig. 6c, and Supplementary Fig. 23). However, visible structural differences are observed in VP35c and VP35d between the two polymerases. In MARV, the C-terminus of mVP35c CR features a short α-helix (residues 163–168) that forms hydrophobic interactions with MARL (I164, F165, L168 of mVP35c with L674 of MARL) (Fig. 6a, c). In contrast, the corresponding region in eVP35c CR is a disordered loop (Fig. 6a), which interacts with EBOL through a single hydrogen bond between Y176 of eVP35c and Q671 of EBOL (Fig. 6c). Notably, superposing eVP35 onto MARL causes atomic clashes (Y176 of eVP35c with Y706 of MARL) (Fig. 6c). Furthermore, the secondary structural differences in the VP35d CRs were also observed between MARV and EBOV, with the interactions among the CRs of VP35c, VP35d and NTD of L present in MARV but absent in EBOV (Fig. 6a, d). These differences in secondary structure and interaction type weaken heterologous VP35–L binding. Additionally, distinct interaction patterns were also observed between VP35d IID and the NTD of L. In MARV, T219 of mVP35d IID not only forms hydrogen bonds with Y331 and Q360 of MARL, but also interacts with a hydrophobic cluster (I327, I355, V359) of MARL (Fig. 6e). In EBOV, the equivalent D230 of eVP35d IID engages in several polar interactions, including a salt bridge with R349 and hydrogen bonds with H324, R353, and R357 of EBOL (Fig. 6e). These differences suggest that the interchange of VP35 molecules significantly disrupts the compatibility of VP35 IID with the NTD of L.

The potential nucleoprotein binding site on VP35

As a polymerase cofactor, VP35 in filoviruses is equivalent to the P protein in other nsNSVs[10,36]. The P protein harbors a C-terminal X domain (XD) that is composed of three α-helices in a number of viruses, including measles[40], Henipa[41], NDV[3], PIV5[29], hPIV3[30], MuV[31], etc. The XD of P protein (P_{XD}) could associate with L and the molecular recognition element (MoRE) of the N protein (N^{MoRE}), which ensures the polymerase complex to attach to and slide along the RNP template during RNA synthesis. Further inspection of the longest VP35 molecules in the polymerase complexes revealed a four-helix bundle in the N lobe of the IID, in which the P_{XD} in complex with N^{MoRE} from either measles or Nipah virus could be superimposed onto that of both MARV and EBOV polymerases (Fig. 7a, b and Supplementary Fig. 24a, b). However, the N^{MoRE} of both measles and Nipah viruses occupy the position that overlapped with α7 of VP35 (Fig. 7a, b and Supplementary Fig. 24a, b). In the IID of eVP35, the first basic patch that comprising residues R225, H240, K248 and K251 has been identified as crucial for nucleoprotein association and vital for viral RNA synthesis[14]. These residues are highly conserved among the Ebola viruses but showed some alterations in Marburg genus (Supplementary Fig. 21), as the corresponding residues R225 and K251 have varied into A214 and Y240 respectively in mVP35 during evolution (Fig. 7c). These residues lie on the exposed surface of IID and are close to the NTP entry channel (Fig. 7c), suggesting that NP binding may not require a conformational change or structural remodeling of the polymerase complex. However, in the cryo-EM structure of PIV5 and NDV, the N^{MoRE} binding sites are located on the other side of the three-helical bundle when the structures of P_{XD}–N^{MoRE} from these two viruses are superimposed (Supplementary Fig. 24c–f). Hence, both VP35 molecules in filoviruses contain cryptic N^{MoRE}-like binding sites in their IIDs, which are distinct from paramyxoviruses. Furthermore, superimposition of the dsRNAs onto the central basic patches of IIDs does not generate steric hindrance with L in both EBOV and MARV (Supplementary Fig. 25), suggesting

https://doi.org/10.1038/s41467-025-58308-1

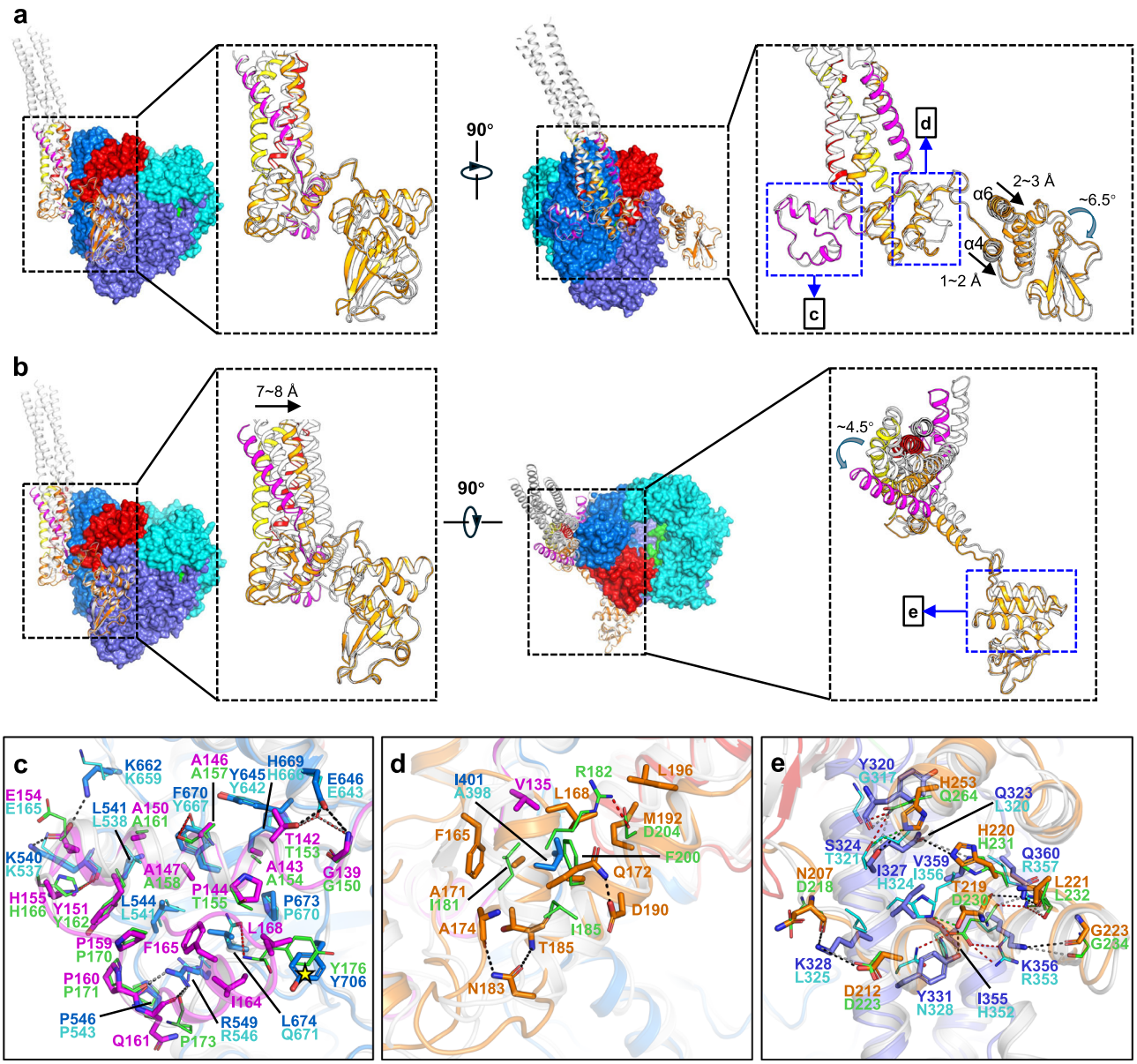

Fig. 6 | Comparison of L–VP35 interactions between MARV and EBOV polymerases. a Superimposition of eVP35 (PDB: 7YER) onto mVP35 (this work) based on the alignment of OD and CR. MARL and mVP35 are shown and colored the same as in Fig. 5a. eVP35 is shown as ribbon and colored in white. A 6.5° rotation between eVP35 and mVP35 IIDs and the distances of α4 and α6 movements are indicated. **b** Superimposition of eVP35 (PDB: 7YER) onto mVP35 (this work) based on the alignment of IID. A 7–8 Å shift and 4.5° rotation between eVP35 and mVP35 ODs are indicated. **c**–**e** Zoom-in views of the blue boxes in **a** and **b**. MARL and mVP35 tetramer are depicted as ribbon and colored as in Fig. 5. EBOL and eVP35 are shown in light gray ribbons. Residues that involved in the interactions between MARL and mVP35 are shown as sticks. Residues that involved in the interactions between EBOL and eVP35 are shown in lines. Polar interactions between MARL and mVP35 are represented by black dashed lines, and those between EBOL and eVP35 are displayed by red dashed lines. Putative polar interactions between MARL and eVP35 are represented by gray dashed lines, and those between EBOL and mVP35 are represented by green dashed lines. The yellow pentacle indicates the predicted clash between Tyr176 of eVP35 and Tyr706 of MARL.

that the dsRNA binding and IFN suppression properties of VP35 may not be influenced upon engagement with L.

Discussion

Filoviruses require both L protein and VP35 to form functional polymerase complexes to perform replication and transcription during viral life cycle[2,5]. In this study, we determined the high-resolution cryo-EM structures of L–VP35 complexes for both MARV and EBOV, two highly lethal filoviruses in the order *Mononegavirales*. Despite similar overall architectures, indicative of conserved assembly mechanisms across filoviruses, we uncovered virus-specific L–VP35 interactions unique to each virus. Notably, the EBOV polymerase structure we present here exhibits a contracted conformation that has not been described before, characterized by a shrunken central cavity and a narrowed template entry channel, suggesting a distinct state in the RNA synthesis process. Intriguingly, despite the striking similarity in suramin-binding sites between the EBOV and MARV polymerases, suramin showed significantly lower binding affinity for the MARV polymerase compared to the EBOV polymerase. This discrepancy suggests subtle structural differences between the RNA polymerases of these closely related filoviruses. Consequently, the development of MARV RNA polymerase inhibitors cannot simply replicate the strategies used for EBOV polymerase inhibitors. All these findings enhance our understanding in the replication and transcription mechanisms of

https://doi.org/10.1038/s41467-025-58308-1

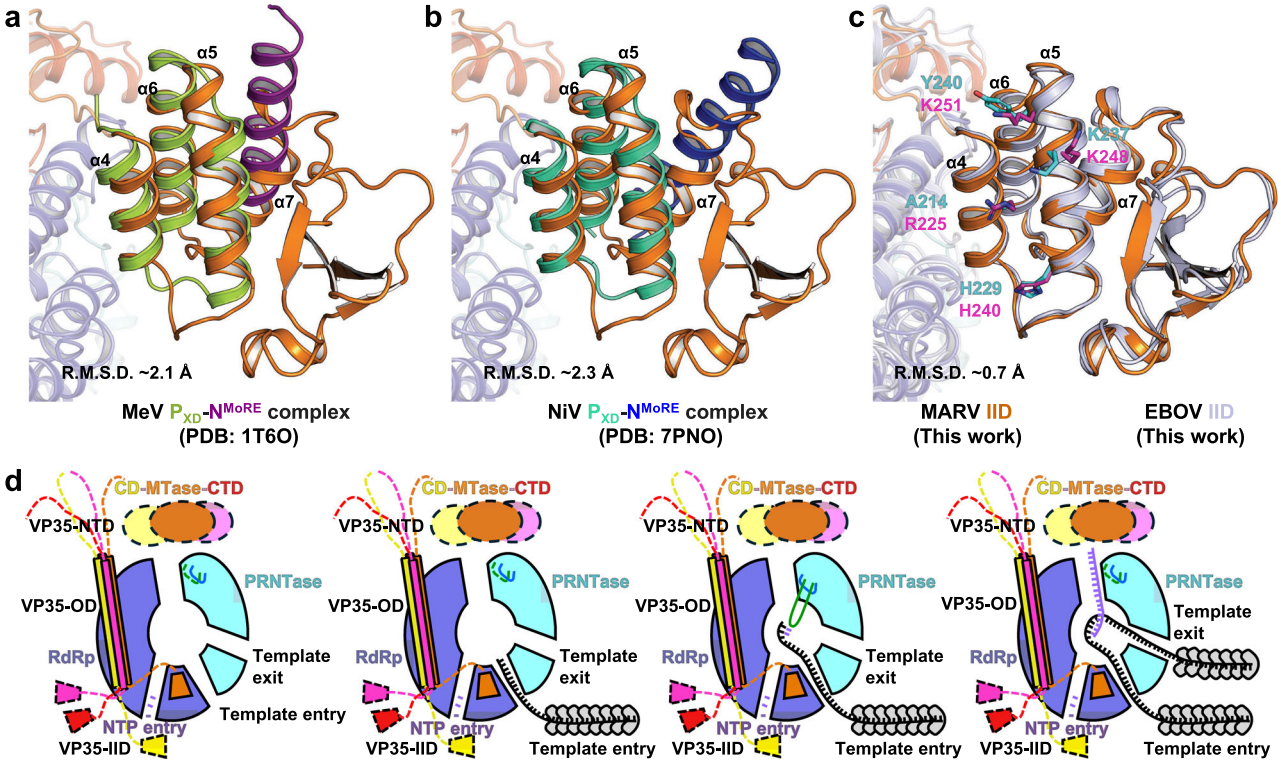

Fig. 7 | The potential nucleoprotein (NP) binding site on VP35. a, b Superimposition of the MeV (measles virus) P_{XD}–N^{MoRE} complex (PDB: 1T6O) (**a**) and the NiV (Nipah virus) P_{XD}–N^{MoRE} complex (PDB: 7PNO) (**b**) onto the mVP35 IID of MARV polymerase complex. **c** Superimposition of VP35 IIDs from MARV and EBOV polymerases determined in this study. Key residues reported for NP–VP35 IID interactions are shown as sticks and colored by cyan (mVP35) and magenta (eVP35), respectively. The P_{XD} and N^{MoRE} of MeV are colored in limon and purple, respectively and the P_{XD} and N^{MoRE} of NiV are shown in lime green and dark blue, respectively. mVP35d IID is shown in orange and eVP35d IID in blue-white. **d** The proposed model for RNA synthesis by filovirus polymerases. Briefly, in the apo state without RNA binding (I), the priming loop of the filovirus polymerase is ordered or partially ordered, while the instruction loop is retained in the PRNTase domain. In the pre-initiation state once the replication promoter is bound to the polymerase (II), the recognition of the promoter RNA does not seem to affect the conformation of the priming loop and the instruction loop in filoviruses. In the initiation state (III), the priming loop inserts into the catalytic cavity, and an aromatic or ring-based residue from the loop may participate in the stabilization of the first two nucleotide to facilitate the formation of the first phosphodiester bond[11,65]. With the incorporation of more NTPs into the nascent RNA, the RNA product grows longer, and the polymerase gradually enters an elongation state (IV), in which both the priming loop and the instruction loop are retracted into the PRNTase domain or even completely disordered, allowing the RNA product to pass through the product exit channel.

filovirus polymerases and provide critical insights for developing effective antiviral drugs against these lethal pathogens.

VP35 serves as a pivotal antagonist to the host innate immune response and as an indispensable cofactor for the L polymerase, functionally paralleling the P protein in other nsNSVs. Previous studies on eVP35 and mVP35 suggested distinct RNA binding preference and efficiency of antagonizing immune response mediated by their IIDs[42–44]. In addition, homo-oligomerization of VP35 through ODs is essential for its function in viral replication and transcription as well as maximizing the interferon-antagonist activity[13,45]. So far, different oligomerization states of VP35 proteins have been revealed by the crystal structures that eVP35 can be either packed into a trimer or tetramer[16] while mVP35 forms a trimer[15]. However, in our cryo-EM structure of MARV L–VP35 complex determined here, four mVP35 molecules with different lengths have been observed and each assumes as a distinct conformation, similar to the tetrameric assembly of eVP35 in the EBOV L–VP35 complex structures[8,9], which suggests that the assembly of the polymerase complex is highly conserved among the filoviruses. Although the modeled residues of mVP35 OD in our cryo-EM structure (residues 113–135) overlap with the coiled coil (residues 60–135) in the C-terminal portion of the crystal structure, the trimer could not be superimposed onto the tetrameric mVP35 in our model. Thus, it is plausible that mVP35 experiences oligomerization remodeling upon binding to MARL or the trimeric structure may result from crystal packing if it forms a tetramer in solution. Furthermore, the observed length of OD of mVP35 in the cryo-EM structure is much shorter than that of eVP35 or the P proteins in the polymerase complexes of EBOV, PIV5 and MuV[8,9,29,31] (Supplementary Fig. 10). The variances in the ODs are also reflected in the 2D class averages of these polymerases (Supplementary Fig. 2–4), in which a turn is observed in mVP35 OD, indicating greater flexibility in the OD of mVP35 compared to eVP35. These findings, together with various oligomerization states of VP35 in different filoviruses[16], imply that the differences in VP35 dynamics among the filoviruses may dictate the potential divergent mechanisms of replication and pathogenesis during viral propagation.

Surprisingly, virus-specific L–VP35 interactions are observed within the structures of the EBOV and MARV polymerase complexes (Fig. 6), although the sequence similarity of their L and VP35 is relatively high (Supplementary Fig. 13, 21). In addition, our pull-down experiments reveal the reduced affinity and the failure of heterologous L and VP35 to assemble into the complete polymerase complexes between MARV and EBOV (Supplementary Fig. 22), and it can't exclude the possibility that the resulting chimeric polymerase complexes would compromise the binding of NP to heterologous VP35, both of which confirms the previous observation that interchanging L or VP35 could not support the reporter gene expression in the replication systems[19]. Furthermore, the nucleocapsid proteins of EBOV and MARV are also not interchangeable in the recombinant minigenome assays[19], indicating the interactions among the NP and L–VP35 should be highly specific to each virus. And in our structures, we also observed that the

potential NP-binding sites on VP35 proteins are also not completely conserved between MARV and EBOV. Moreover, MARV VP30 was shown to be able to substitute EBOV VP30 for transcriptional activation of reporter gene expression, although with reduced efficiency[19]. Analogously, the complex structures of P_{XD} and N^{MoRE} from Sendai and measles viruses are highly similar, however, their interaction interfaces as well as the affinities of each protein pair differ greatly[46]. Therefore, the prerequisite for these heterologous viral proteins to function in different species is likely to be their ability to recognize their respective partners specifically and form functional complexes under the given expression system. Hence, our structural study on L–VP35 interaction of MARV illustrates divergence in polymerase complex formation during the adaptation and evolution of the filoviruses and elucidates how selection pressure enables L, VP35 and their partners to evolve concomitantly within the filovirus family with similar sequences and conserved structures, which might imply the potential discrepancies in the mechanisms during RNA synthesis and pathogenicity.

L–VP35 complex functions as a versatile RNA-dependent RNA polymerase, capable not only of replicating the entire viral genome and transcribing mRNAs, but also of performing modifications on the nascent RNAs including capping, methylation and the addition of polyadenylated tails through intricate mechanisms and multiple processes[2]. Thus, the polymerase must undergo various states and conformational changes during different catalytic stages of viral RNA synthesis. It is widely accepted that the two loops, the priming and the intrusion loops protruding from the PRNTase domain and maybe the supporting helix from the palm catalytic subdomain are related to the RNA synthesis state of the polymerase[10,36]. To date, only limited states of the L–P complexes from the nsNSVs have been reported, including the polymerases of VSV and RABV from the rhabdovirus family in the initiation state[26,28], the polymerases of PIV3, PIV5, MuV and NDV from the paramyxovirus family in the post- or non-initiation state[26–29], the polymerases of RSV and HMPV from the human metapneumovirus family as well as the polymerases of EBOV and MARV from the filovirus family in the elongation state[8,32–34] (Fig. 3 and Supplementary Fig. 15c–e).

Recently, two studies reported the pre-initiation state of the EBOV and RSV polymerase complexes, in which the replication promoters (either leader or trailer) from the viral genomes were bound to the template entry channels with certain nucleotides in the promoters were specifically recognized by the residues within the RNA entry channels[9,35]. Upon promoter binding, RSV polymerase experiences conformational changes including the stabilization of the supporting helix and the supporting loop as well as subtle inward movement of the PRNTase domain[35], whereas there is no obvious overall structural remodeling of EBOV polymerase upon the association of the 3′-leader[9]. Interestingly, our cryo-EM structure of MARV in the apo-form could be well superimposed with the leader-bound EBOV polymerase in the pre-initiation state, in the template entry channel, the residues that interact with the replication promoter sequence are highly conserved between these two viruses (Supplementary Fig. 16e).

It is worth noting that the 3′-leader or trailer sequence of MARV is similar to that of EBOV. Specifically, the de novo initiation site (+1 position) of the MARV 3′-trailer sequence is identical to that of EBOV promoter except that EBOV leader or trailer contains an additional G/A at the extreme 3′ end of the genome (Supplementary Fig. 16f). Furthermore, it has been reported that both MARV and EBOV polymerases initiate RNA synthesis at +2 position on the EBOV 3′-leader[22]. Therefore, our MARV structure could take advantage of the leader-bound EBOV polymerase structure to mimic the pre-initiation state of MARV polymerase. The first 2 nucleotides of the RNA product could be modeled complementary to the +2 and +3 positions of the EBOV leader RNA in EBOV and MARV polymerases (Supplementary Fig. 26a, b) or to the +1 and +2 position of the MARV trailer RNA in the MARV polymerase (Supplementary Fig. 26c). These dinucleotides are located opposite to the GDN catalytic residues from the palm subdomains, corresponding to the −1 and +1 catalytic sites where the phosphodiester bond is formed (Supplementary Fig. 26a–c). The modeling of the RNA products in EBOV and MARV polymerases not only illuminates the potential mechanism of de novo RNA synthesis on replication promoters but also accounts for the previous biochemical observations that EBOV polymerase initiates RNA synthesis from the +2 position of the RNA template while MARV polymerase initiates from the +1 position of its own promoter but from position 2 on the EBOV promoter[22,23] (Supplementary Fig. 26a, c). Thus, due to lack of an additional G/A nucleotide at the 3′ end of the MARV genome, the +2 position on the EBOV replication promoter corresponds to the +1 position on the MARV replication promoter. In addition, our modeling partially explains the observation that the MARV polymerase is capable of recognizing and utilizing the leader sequences from both its own genome and the EBOV genome for replication and transcription in minigenome assays[19]. However, it remains unclear why the EBOV polymerase is unable to employ the MARV promoter for RNA synthesis although the first two nucleotides in the template have no direct contact with EBOL protein in the cryo-EM structure[9] (Supplementary Fig. 16b), implying that the nucleotides in the +1 and +2 positions of the leader might be specifically recognized by the EBOL in certain catalytic steps. Moreover, whether the polymerases have a preference for the initiating nucleotide and how they stabilize the first nucleotide during de novo RNA synthesis still need to be further investigated.

During the polymerase transition from the initiation state to the post-initiation and elongation state, the nascent RNA product gradually grows longer with the addition of the incoming nucleotides, which is accompanied by the conformational changes of the priming and intrusion loops as well as the supporting helix to coordinate the RNA synthesis process (Fig. 7d). Of note, to comprehensively understand the bona fide post-initiation and elongation states for the polymerases of the nsNSVs, it is still necessary to determine high-resolution structures of the polymerases in complex with the corresponding RNA templates and products.

It is highly intriguing that the accessory regions of the L proteins of nsNSVs, encompassing the connection domain, methyltransferase domain and the C-terminal domain, are not always visible in the solved cryo-EM structures. Particularly, the cryo-EM structures of polymerases from filovirus and human metapneumovirus have no densities for the accessory regions in their L proteins even if the full-length L proteins are used for sample preparation and structural determination[8,9,32–35], whereas the accessory regions attached to the core region can be observed in the structures of paramyxoviral and rhabdoviral polymerases[3,26–31]. It is possible that the accessory regions of different viruses have different affinity to their core regions in the apo form and this affinity for filovirus and human metapneumovirus may be lower than that for the other nsNSVs, that's why we and others were unable to solve the structures of the accessory regions for MARV and EBOV[8,9]. Therefore, we obtained nearly identical cryo-EM structures for the MARV polymerase when full-length or core region of L protein was used for sample preparation under the same condition. Surprisingly, the cryo-EM structure of EBOV core region we determined here is significantly different from the published one, in which the full-length EBOL was assembled with eVP35 during expression. We speculate that this difference may result from the varying experimental conditions, including the buffers used during the sample preparation (i.e. buffer pH, salt concentration or other compositions) or the disparate vitrification condition (i.e. types of grids, additives and blotting procedure) from respective laboratories.

In our EBOV polymerase structure, the positions of the priming and intrusion loops and the supporting helix are similar to those of other nsNSV polymerase structures in the elongation state[36], suggesting that the structure we obtained also belongs to the elongation

state. Relative to previously published EBOV polymerase structures in the elongation state (apo form)[8], each domain in our structure undergoes a slight inward rotation, resulting in a much more compact conformation and leading to a narrower template entry channel and a smaller central catalytic cavity (Fig. 4 and Supplementary Fig. 18). These conformational variances among the EBOV polymerase structures underscore the polymerase's inherent flexibility and dynamism, necessitating coordinated movements of various domains to facilitate substrate binding and execute complex catalytic activities during RNA synthesis. Observations from the RSV polymerase indicate that upon engagement with leader or trailer RNA, an inward shift of the PRNTase domain occurs, leading to a contracted catalytic pocket[35]. Additionally, in the polymerase of nsNSV, the palm subdomain is flanked by a conserved GGxxG motif on one side and a glycine residue between motif D and E on the other, which may confer relative flexibility between the palm subdomain and other domains. Similar conformational changes among domains of the RNA polymerases during catalysis have also been visualized in a number of viruses, including the influenza virus[47,48], Thogoto virus[49], Hantaan virus[50], Lassa virus[51], La Crosse virus[52], hepatitis C virus[53] and SARS-CoV-2[54–56]. These instances further delineate the critical role of domain flexibility and synergy during substrate binding and catalysis by these polymerases. The compact conformation of EBOV polymerase we obtained here may also represent a specific state in the catalytic cycle, which might be adopted by other nsNSVs as well. In addition, it does not exclude the possibility that the conformational changes of the polymerase through rhythmic relaxation and contraction, also known as "molecular respiration", facilitates the template RNA to be continuously squeezed into the catalytic pocket and also plays a role in the translocation of the template during RNA synthesis.

In conclusion, we have determined the high-resolution cryo-EM structures of L–VP35 complexes for both MARV and EBOV, two highly lethal filoviruses in the order *Mononegavirales*. The differences in L–VP35 interactions between MARV and EBOV, as well as the variations among EBOV polymerase structures, broaden our understanding of how these polymerase complexes assemble and function during replication. Our findings also provide mechanistic insights into the initiation and elongation processes during RNA synthesis, which are crucial for the development of potent antiviral drugs against these highly lethal Ebola and Marburg viruses, as well as other nsNSVs.

Methods

Cloning, protein expression and purification

Codon-optimized MARV L (UniProtKB/Swiss-Prot: P31352), MARV VP35 (UniProtKB/Swiss-Prot: P35259), EBOV L (UniProtKB/Swiss-Prot: Q05318) and EBOV VP35 (UniProtKB/Swiss-Prot: Q05127) genes were individually subcloned into modified pFastBac1 vectors (Thermo Fischer Scientific). For MARV, the full-length or truncated MARV L (residues 1–1425) were subcloned with a C-terminal 2×Strep-His_6-MBP-Flag tag and the full-length or truncated mVP35 (residues 57–329) carried an N-terminal His_6-MBP tag. Both full-length and truncated MARV polymerase complexes were produced by co-expression of MARL and mVP35 in the baculovirus expression system according to the Bac-to-Bac instructions (Thermo Fischer Scientific). For purification, the Sf9 cells (Thermo Fischer Scientific, Cat# 11496015) were harvested by centrifugation at 3,220 *g* for 20 min at 4 °C 72 h after infection. The cell pellet was resuspended in lysis buffer A_1 (25 mM HEPES, pH 7.5, 500 mM NaCl, 1 mM Tris (2-carboxyethyl) phosphine (TCEP)) supplemented with EDTA-free Protease Inhibitor Cocktail (Selleck). Cells were lysed by sonication, and cell debris were removed by centrifugation at 16,300 *g* for 45 min at 4 °C. The clarified lysate was incubated with pre-equilibrated anti-FLAG G1 affinity resin (GenScript Biotech) for 2 h at 4 °C. The resin was collected by centrifugation at 500 *g* for 5 min at 4 °C and loaded onto a gravity flow column. The resin was then washed by 100 column volumes of buffer A_1 and the bound proteins were eluted by the buffer A_1 containing 200 μg/mL FLAG peptide. The eluted proteins were concentrated using a 100 kDa cutoff centrifugal filter (Millipore) and subjected to size exclusion chromatography (SEC) on a Superose 6 Increase 10/300 GL column (Cytiva) pre-equilibrated by buffer A_1 supplemented with 6 mM $MgCl_2$. Peak fractions containing the target proteins were pooled and concentrated to ~1.2 mg/mL prior to cryo-EM studies.

The EBOV polymerase complexes were produced by the similar strategy. Briefly, the full-length or truncated EBOV L (residues 1–1400) with an N-terminal 2×Strep-His_6-MBP-Flag tag were co-expressed with the full-length or truncated eVP35 (residues 80–340) with an N-terminal His_6-MBP tag. Streptavidin beads (Smart-Lifesciences) were used to enrich the EBOV polymerase complexes. The beads were washed by buffer A_1 and the bound EBOV polymerase complexes were eluted by buffer B_1 containing 25 mM HEPES, pH 7.5, 300 mM NaCl, 1 mM TCEP supplemented with 2.5 mM desthiobiotin. After concentration, the proteins were further purified and homogenized by the same gel filtration column as MARV polymerase complexes in buffer B_1 supplemented with 6 mM $MgCl_2$. The peak fractions were pooled and concentrated to ~1.2 mg/mL prior to cryo-EM studies.

To conduct the VP35 interchange experiment, full-length MARL or EBOL was co-expressed with either full-length mVP35 or eVP35 and the homologous and heterologous complexes were purified by the similar protocols mentioned above for obtaining the L–VP35 complexes. The eluted complexes were then analyzed by SDS-PAGE.

In order to examine the bipartite binding of OD + CR and IID of VP35 to the L protein respectively, mVP35 OD + CR (residues 57–207) and IID (residues 208–329) were individually subcloned into modified pFastBac vectors (Thermo Fisher Scientific), each carrying an N-terminal His_6-MBP tag. Full-length MARL was co-expressed either with mVP35 OD + CR alone or with mVP35 OD + CR and IID together. The complexes were purified by the similar procedures mentioned above for obtaining these L–VP35 complexes. The eluted complexes were then analyzed by SDS-PAGE and size-exclusion chromatography using a Superose 6 Increase 10/300 GL column (Cytiva).

To measure the binding affinity of suramin to both MARV and EBOV polymerases, full-length MARL or EBOL with a C-terminal eGFP tag was co-expressed with either truncated mVP35 or eVP35, and the complexes were purified by the similar protocols mentioned above for obtaining the fluorescently-labeled L–VP35 complexes. The concentrations of the protein samples were quantified by the absorption at 280 nm.

Cryo-EM sample preparation

For cryo-EM sample preparation, 3 μL of the $(L–VP35)_M^{FL}$ complex at the concentration of ~1.2 mg/mL was applied to a glow-discharged NiTi-Cu grid (1.2/1.3, 300 mesh) (Guangzhou Najing Dingxin Technology). Additives including either 0.05% CHAPS or 2% trehalose was applied to partially alleviate the denaturing of the complex adsorbed at the air–water interface for the $(L–VP35)_M^{FL}$ sample. For $(L–VP35)_M^{Core}$ and $(L–VP35)_E^{Core}$, 3 μL samples without additives were applied to NiTi-Au grids (1.2/1.3, 300 mesh). Grids were blotted for 3.0 s or 3.5 s with a humidity of 100% at 4 °C and plunge-frozen into liquid ethane using a Vitrobot Mark IV (Thermo Fischer Scientific).

Cryo-EM data acquisition

The cryo-EM data of $(L–VP35)_M^{FL}$ and $(L–VP35)_M^{Core}$ were collected at the Cryo-Electron Microscopy Facility of Hubei University. Micrographs were collected on a 300 kV Titan Krios microscope equipped with a BioQuantum energy filter. EPU software was used for automated data collection according to standard procedures. The movie stacks were recorded using a K3 Summit detector (Gatan) in counting mode. Datasets were collected at a magnification of 105,000×, corresponding to a calibrated pixel size of 0.851 Å. Each micrograph was dose-fractionated to 40 frames at a dose rate of 15.156 e^- per pixel

per second, with a total exposure time of 2.5 s, resulting in a total dose of about 52.52 $e^-/Å^2$. The defocus range was set from −1.0 to −1.5 µm. A total of 6388 movies were recorded for $(L–VP35)_M^{FL}$ and 2,023 movies for $(L–VP35)_M^{Core}$ with the same settings for the parameters.

The cryo-EM data of $(L–VP35)_E^{Core}$ was collected at the Center of Cryo-Electron Microscopy at Zhejiang University. Data collection was performed on a Titan Krios (Thermo Fischer Scientific) electron microscope operated at 300 kV equipped with Gatan Falcon 4 detector. Datasets were collected at a magnification of 130,000×, corresponding to a calibrated pixel size of 0.93 Å. Each micrograph was dose-fractionated to 40 frames at a dose rate of 9.6 e^- per pixel per second, with a total exposure time of 4.5 s, resulting in a total dose of about 50 $e^-/Å^2$. The defocus range was set from −1.0 to −1.8 µm. A total of 1307 movies were collected for the following processing. The statistics of cryo-EM data collection are summarized in Supplementary Table 1.

Image processing

All data processing procedures were conducted using cryoSPARC (v4.2.1)[57]. Each dataset was initially processed for motion correction and contrast transfer function (CTF) estimation. For $(L–VP35)_M^{FL}$, a total of 2,102,498 particles were autopicked using blob picker and then extracted with a box size of 360 pixels. Following particle extraction, multiple rounds of 2D classification were performed, each producing 96 distinct classes. In the final round of 2D classification, 17 class averages with clear features were selected as a reference for template picker. Then a total of 4,054,577 particles were re-extracted and finally 822,647 particles were selected for ab-initio reconstruction after multiple rounds of 2D classification. After two rounds of heterogeneous refinements, one class with better resolution was subjected to non-uniform refinement and finally a 2.68-Å resolution map was generated.

For datasets $(L–VP35)_M^{Core}$ and $(L–VP35)_E^{Core}$, the processing procedures were similar. After motion correction and CTF estimation, 2,720,340 and 3,415,582 particles were template-picked using the above MARV and previously published EBOV maps as references, respectively. Following two rounds of 2D classification, 208,094 and 152,620 particles were selected for ab-initio reconstruction, respectively. The best subsets, comprising 178,297 and 77,587 particles, were then subjected to non-uniform refinement to yield the maps with resolutions at 2.84 Å and 3.11 Å, respectively. All refinements follow the gold-standard procedure, in which two half datasets were refined independently, and the resolutions were estimated based on the Fourier shell correlation (FSC) = 0.143 criterion.

Model building and refinement

To obtain the atomic models for MARV and EBOV polymerase complexes, the cryo-EM maps at atomic or near-atomic resolutions were used for automated and de novo model building by ModelAngelo[58]. Manual adjustments were performed in COOT[59] and the models were refined in real and reciprocal spaces iteratively in PHENIX[60], using artificial unit cells, electron scattering factors, secondary-structure and Ramachandran restraints. The final models were validated by MolProbity[61].

Microscale thermophoresis (MST) binding assay

The MST binding assay was applied to measure the affinity of suramin molecule to EBOV and MARV polymerases. Both purified EBOV and MARV polymerases labeled with C-terminal eGFP fusions on the L subunits were served as targets. For all interactions, 16 serially diluted titrations of suramin (concentration ranging from 30 nM to 1 mM) were mixed with a fixed concentration (50 nM) of the eGFP-labeled polymerases in the buffer containing 20 mM HEPES, pH 7.5, either 150 or 500 mM NaCl, 1 mM TCEP and 0.05% Tween 20. Samples were loaded into 5 µL standard-treated capillaries (Hirschmann, Germany) after the reactions were incubated in the dark at 25 °C for 30 min to 1 h. Then the samples were mounted in a Monolith NT.115 instrument with blue/red filters (NanoTemper Technologies, Germany) for binding measurements, which were performed at 25 °C using 20% blue LED excitation power (blue filter, excitation 460–480 nm, emission 515–530 nm) and 60% IR-laser power with off/on times of 3 s and 20 s. 16 titrations were measured to generate one full binding isotherm and all experiments were repeated three times for each measurement. Data analyses were performed using the NanoTemper analysis software. The K_d constants between EBOV and MARV polymerases and suramin were calculated using the saturation binding curve at equilibrium. For MARV polymerase, only a lower bound of a K_d value was possible to estimate, owing to a lack of saturation in the binding isotherm. For such cases, a mean K_d was not determined. All measurements were performed in biologically independent triplicates. The raw data are provided in the Source Data file.

Figure preparation

The analysis of MARV and EBOV L–VP35 interactions were carried out using PyMOL (https://pymol.org/2/) and PDBePISA (https://www.ebi.ac.uk/pdbe/pisa/). All the figures representing the models and electron density maps were prepared using UCSF Chimera, ChimeraX[62] and PyMOL. Multiple sequence alignments were performed using Multalin[63] and ESPript[64].

Reporting summary

Further information on research design is available in the Nature Portfolio Reporting Summary linked to this article.

Data availability

The authors declare that all data supporting the findings of this study are available in the article, its Supplementary Information, and its Source Data. The cryo-EM maps and atomic coordinates generated in this study have been deposited to the Electron Microscopy Data Bank (EMDB) and the Protein Data Bank (wwwPDB), respectively. The accession codes are as follows: EMD-60755 and PDB 9IP2 for $(L–VP35)_M^{FL}$; EMD-60756 and PDB 9IP3 for $(L–VP35)_E^{Core}$; and EMD-60757 and PDB: 9IP4 for $(L–VP35)_M^{Core}$. In addition, previously published structural models were used for comparison in this study. The corresponding PDB accession codes are: 1N6B, 1T6O, 3L25, 4GHL, 5A22, 6OGZ, 6PZK, 6U1X, 6U5O, 6UEB, 6V85, 7PNO, 7YER, 7YES, 7YET, 7YOU, 8IZL, 8JSL, 8KDB, 8KDC, 8SNX and 8SNY. Source data are provided with this paper.

References

1. Amarasinghe, G. K. et al. Taxonomy of the order Mononegavirales: update 2019. *Arch. Virol.* **164**, 1967–1980 (2019).
2. Hume, A. J. & Muhiberger, E. Distinct Genome Replication and Transcription Strategies within the Growing Filovirus Family. *J. Mol. Biol.* **431**, 4290–4320 (2019).
3. Cong, J. et al. Structure of the Newcastle Disease Virus L protein in complex with tetrameric phosphoprotein. *Nat. Commun.* **14**, 1324 (2023).
4. Cross, R. W., Mire, C. E., Feldmann, H. & Geisbert T. W. Post-exposure treatments for Ebola and Marburg virus infections. *Nat. Rev. Drug Discov.* **17**, 413–434 (2018).
5. Muhlberger, E. Filovirus replication and transcription. *Future Virol.* **2**, 205–215 (2007).
6. Jain, S., Martynova, E., Rizvanov, A., Khaiboullina, S. & Baranwal, M. Structural and Functional Aspects of Ebola Virus Proteins. *Pathogens* **10**, 1330 (2021).
7. Fujita-Fujiharu, Y. et al. Structural insight into Marburg virus nucleoprotein-RNA complex formation. *Nat. Commun.* **13**, 1191 (2022).

8. Yuan, B. et al. Structure of the Ebola virus polymerase complex. *Nature* **610**, 394–401 (2022).
9. Peng, Q. et al. Molecular mechanism of de novo replication by the Ebola virus polymerase. *Nature* **622**, 603–610 (2023).
10. Pyle, J. D., Whelan, S. P. J. & Bloyet, L. M. Structure and function of negative-strand RNA virus polymerase complexes. *Enzymes* **50**, 21–78 (2021).
11. Te Velthuis, A. J. W., Grimes, J. M. & Fodor, E. Structural insights into RNA polymerases of negative-sense RNA viruses. *Nat. Rev. Microbiol* **19**, 303–318 (2021).
12. Becker, S., Rinne, C., Hofsass, U., Klenk, H. D. & Muhlberger, E. Interactions of Marburg virus nucleocapsid proteins. *Virology* **249**, 406–417 (1998).
13. Moller, P., Pariente, N., Klenk, H. D. & Becker, S. Homo-oligomerization of Marburgvirus VP35 is essential for its function in replication and transcription. *J. Virol.* **79**, 14876–14886 (2005).
14. Prins, K. C. et al. Basic Residues within the Ebolavirus VP35 Protein Are Required for Its Viral Polymerase Cofactor Function. *J. Virol.* **84**, 10581–10591 (2010).
15. Bruhn, J. F. et al. Crystal Structure of the Marburg Virus VP35 Oligomerization Domain. *J. Virol.* **91**, e01085-16 (2017).
16. Zinzula, L. et al. Structures of Ebola and Reston Virus VP35 Oligomerization Domains and Comparative Biophysical Characterization in All Ebolavirus Species. *Structure* **27**, 39 (2019).
17. Muhlberger, E., Lotfering, B., Klenk, H. D. & Becker, S. Three of four nucleocapsid proteins of Marburg virus, NP, VP35, and L, are sufficient to mediate replication and transcription of marburg virus-specific monocistronic minigenomes. *J. Virol.* **72**, 8756–8764 (1998).
18. Schmidt, K. M. & Muhlberger, E. Marburg Virus Reverse Genetics Systems. *Viruses-Basel* **8**, 178 (2016).
19. Muhlberger, E., Weik, M., Volchkov, V. E., Klenk, H. D. & Becker, S. Comparison of the transcription and replication strategies of Marburg virus and Ebola virus by using artificial replication systems. *J. Virol.* **73**, 2333–2342 (1999).
20. Sanchez, A., Trappier, S. G., Mahy, B. W. J., Peters, C. J. & Nichol, S. T. The virion glycoproteins of Ebola viruses are encoded in two reading frames and are expressed through transcriptional editing. *P Natl Acad. Sci. USA* **93**, 3602–3607 (1996).
21. Edwards, M. R., Vogel, O. A., Mori, H., Davey, R. A. & Basler, C. F. Marburg Virus VP30 Is Required for Transcription Initiation at the Glycoprotein Gene. *Mbio* **13**, e0224322 (2022).
22. Shareef, A. M., Ludeke, B., Jordan, P., Deval, J. & Fearns, R. Comparison of RNA synthesis initiation properties of non-segmented negative strand RNA virus polymerases. *Plos Pathog.* **17**, e1010151 (2021).
23. Deflubé, L. R. et al. Ebolavirus polymerase uses an unconventional genome replication mechanism. *P Natl Acad. Sci. USA* **116**, 8535–8543 (2019).
24. Chen, J., Noble, A. J., Kang, J. Y. & Darst, S. A. Eliminating effects of particle adsorption to the air/water interface in single-particle cryo-electron microscopy: Bacterial RNA polymerase and CHAPSO. *J. Struct. Biol. X* **1**, 100005 (2019).
25. Li, B., Zhu, D., Shi, H. & Zhang, X. Effect of charge on protein preferred orientation at the air-water interface in cryo-electron microscopy. *J. Struct. Biol.* **213**, 107783 (2021).
26. Liang, B. et al. Structure of the L Protein of Vesicular Stomatitis Virus from Electron Cryomicroscopy. *Cell* **162**, 314–327 (2015).
27. Jenni, S. et al. Structure of the Vesicular Stomatitis Virus L Protein in Complex with Its Phosphoprotein Cofactor. *Cell Rep.* **30**, 53 (2020).
28. Horwitz, J. A., Jenni, S., Harrison, S. C. & Whelan, S. P. J. Structure of a rabies virus polymerase complex from electron cryo-microscopy. *Proc. Natl. Acad. Sci. USA* **117**, 2099–2107 (2020).
29. Abdella, R., Aggarwal, M., Okura, T., Lamb, R. A. & He, Y. Structure of a paramyxovirus polymerase complex reveals a unique methyltransferase-CTD conformation. *Proc. Natl Acad. Sci. USA* **117**, 4931–4941 (2020).
30. Xie, J. et al. Structural basis for dimerization of a paramyxovirus polymerase complex. *Nat. Commun.* **15**, 3163 (2024).
31. Li, T. et al. Structures of the mumps virus polymerase complex via cryo-electron microscopy. *Nat. Commun.* **15**, 4189 (2024).
32. Pan, J. et al. Structure of the human metapneumovirus polymerase phosphoprotein complex. *Nature* **577**, 275–279 (2020).
33. Gilman, M. S. A. et al. Structure of the Respiratory Syncytial Virus Polymerase Complex. *Cell* **179**, 193–204 e114 (2019).
34. Cao, D. et al. Cryo-EM structure of the respiratory syncytial virus RNA polymerase. *Nat. Commun.* **11**, 368 (2020).
35. Cao, D. et al. Structures of the promoter-bound respiratory syncytial virus polymerase. *Nature* **625**, 611–617 (2024).
36. Ouizougun-Oubari, M. & Fearns, R. Structures and Mechanisms of Nonsegmented, Negative-Strand RNA Virus Polymerases. *Annu. Rev. Virol.* **10**, 199–215 (2023).
37. Mastrangelo, E. et al. Structure-based inhibition of Norovirus RNA-dependent RNA polymerases. *J. Mol. Biol.* **419**, 198–210 (2012).
38. Yin, W. et al. Structural basis for inhibition of the SARS-CoV-2 RNA polymerase by suramin. *Nat. Struct. Mol. Biol.* **28**, 319–325 (2021).
39. Ogino, T. & Green, T. J. RNA Synthesis and Capping by Non-segmented Negative Strand RNA Viral Polymerases: Lessons From a Prototypic Virus. *Front. Microbiol.* **10**, 1490 (2019).
40. Du Pont, V., Jiang, Y. & Plemper, R. K. Bipartite interface of the measles virus phosphoprotein X domain with the large polymerase protein regulates viral polymerase dynamics. *Plos Pathog.* **15**, e1007995 (2019).
41. Bourhis, J. M. et al. Structural Dynamics of the C-terminal X Domain of Nipah and Hendra Viruses Controls the Attachment to the C-terminal Tail of the Nucleocapsid Protein. *J. Mol. Biol.* **434**, 167551 (2022).
42. Leung, D. W. et al. Structural basis for dsRNA recognition and interferon antagonism by Ebola VP35. *Nat. Struct. Mol. Biol.* **17**, 165–172 (2010).
43. Ramanan, P. et al. Structural basis for Marburg virus VP35-mediated immune evasion mechanisms. *Proc. Natl. Acad. Sci. USA* **109**, 20661–20666 (2012).
44. Edwards, M. R. et al. Differential Regulation of Interferon Responses by Ebola and Marburg Virus VP35 Proteins. *Cell Rep.* **14**, 1632–1640 (2016).
45. Reid, S. P., Cardenas, W. B. & Basler, C. F. Homo-oligomerization facilitates the interferon-antagonist activity of the ebolavirus VP35 protein. *Virology* **341**, 179–189 (2005).
46. Houben, K., Marion, D., Tarbouriech, N., Ruigrok, R. W. & Blanchard, L. Interaction of the C-terminal domains of sendai virus N and P proteins: comparison of polymerase-nucleocapsid interactions within the paramyxovirus family. *J. Virol.* **81**, 6807–6816 (2007).
47. Thierry, E. et al. Influenza Polymerase Can Adopt an Alternative Configuration Involving a Radical Repacking of PB2 Domains. *Mol. Cell* **61**, 125–137 (2016).
48. Kouba, T., Drncova, P. & Cusack, S. Structural snapshots of actively transcribing influenza polymerase. *Nat. Struct. Mol. Biol.* **26**, 460–470 (2019).
49. Xue, L. et al. Cryo-EM structures of Thogoto virus polymerase reveal unique RNA transcription and replication mechanisms among orthomyxoviruses. *Nat. Commun.* **15**, 4620 (2024).
50. Durieux Trouilleton, Q., Barata-Garcia, S., Arragain, B., Reguera, J. & Malet, H. Structures of active Hantaan virus polymerase uncover the mechanisms of Hantaviridae genome replication. *Nat. Commun.* **14**, 2954 (2023).
51. Kouba, T. et al. Conformational changes in Lassa virus L protein associated with promoter binding and RNA synthesis activity. *Nat. Commun.* **12**, 7018 (2021).

52. Arragain, B. et al. Structural snapshots of La Crosse virus polymerase reveal the mechanisms underlying Peribunyaviridae replication and transcription. *Nat. Commun.* **13**, 902 (2022).
53. Mosley, R. T. et al. Structure of hepatitis C virus polymerase in complex with primer-template RNA. *J. Virol.* **86**, 6503–6511 (2012).
54. Gao, Y. et al. Structure of the RNA-dependent RNA polymerase from COVID-19 virus. *Science* **368**, 779–782 (2020).
55. Hillen, H. S. et al. Structure of replicating SARS-CoV-2 polymerase. *Nature* **584**, 154–156 (2020).
56. Peng, Q. et al. Structural and Biochemical Characterization of the nsp12-nsp7-nsp8 Core Polymerase Complex from SARS-CoV-2. *Cell Rep.* **31**, 107774 (2020).
57. Punjani, A., Rubinstein, J. L., Fleet, D. J. & Brubaker, M. A. cryoSPARC: algorithms for rapid unsupervised cryo-EM structure determination. *Nat. Methods* **14**, 290–296 (2017).
58. Jamali, K. et al. Automated model building and protein identification in cryo-EM maps. *Nature* **628**, 450–457 (2024).
59. Emsley, P. & Cowtan, K. Coot: model-building tools for molecular graphics. *Acta Crystallogr D. Biol. Crystallogr* **60**, 2126–2132 (2004).
60. Afonine, P. V. et al. Real-space refinement in PHENIX for cryo-EM and crystallography. *Acta Crystallogr D. Struct. Biol.* **74**, 531–544 (2018).
61. Chen, V. B. et al. MolProbity: all-atom structure validation for macromolecular crystallography. *Acta Crystallogr D. Biol. Crystallogr* **66**, 12–21 (2010).
62. Goddard, T. D. et al. UCSF ChimeraX: Meeting modern challenges in visualization and analysis. *Protein Sci.* **27**, 14–25 (2018).
63. Corpet, F. Multiple Sequence Alignment with Hierarchical-Clustering. *Nucleic Acids Res.* **16**, 10881–10890 (1988).
64. Robert, X. & Gouet, P. Deciphering key features in protein structures with the new ENDscript server. *Nucleic Acids Res.* **42**, W320–W324 (2014).
65. Butcher, S. J., Grimes, J. M., Makeyev, E. V., Bamford, D. H. & Stuart, D. I. A mechanism for initiating RNA-dependent RNA polymerization. *Nature* **410**, 235–240 (2001).

Acknowledgements

We would like to thank the staff at the core facility of Life Sciences Institute (LSI) at Zhejiang University for their technical support, especially Ms. Weina Shang and Ms. Jie Ma for their assistance and advice in the use of the instruments. We are also grateful to the staff of cryo-EM center at Hubei University and Zhejiang University. This work was supported by the National Key Research and Development Program of China (2020YFA0908400 to S.W.), the Distinguished Young Scholars of Hubei Province (2022CFA078 to S.W.), the Knowledge Innovation Program of Wuhan-Shugung Project (2023020201020418 to S.W.), the Young-Thousands Talents Program and the National Natural Science Foundation of China (32371344 to H.R.), as well as the startup funding from LSI, Zhejiang Key Laboratory of Molecular Cancer Biology at Zhejiang University.

Author contributions

H.R. conceived and supervised the study. G.L., T.D., K.J., and Z.R. performed molecular cloning, protein expression, purification and cryo-EM sample preparation. J.W., T.D., and S.W. collected the cryo-EM data. H.R., T.D., and G.L. determined the cryo-EM structures and built the atomic models. X.Z. helped with cryo-EM data processing. T.D. performed MST measurement and data processing. H.R., G.L., and T.D. analyzed the data and wrote the manuscript. L.Z. reviewed the manuscript and contributed valuable suggestions for its revision. All authors participated in discussion and revised the manuscript.

Competing interests

The authors declare no competing interests.

Additional information

Supplementary information The online version contains supplementary material available at https://doi.org/10.1038/s41467-025-58308-1.

Correspondence and requests for materials should be addressed to Shan Wu or Heng Ru.

Peer review information *Nature Communications* thanks Dongchun Ni, and the other, anonymous, reviewers for their contribution to the peer review of this work. A peer review file is available.